

UC Irvine

UC Irvine Previously Published Works

Title

Intravital Vascular Phototheranostics and Real-Time Circulation Dynamics of Micro- and Nanosized Erythrocyte-Derived Carriers

Permalink

<https://escholarship.org/uc/item/9b9490r6>

Journal

ACS Applied Materials & Interfaces, 12(1)

ISSN

1944-8244

Authors

Jia, Wangcun

Burns, Joshua M

Villantay, Betty

et al.

Publication Date

2020-01-08

DOI

10.1021/acsami.9b18624

Peer reviewed

Intravital Vascular Phototheranostics and Real-Time Circulation Dynamics of Micro- and Nano-sized Erythrocyte-Derived Carriers

Wangcun Jia, Joshua Burns, Betty Villantay, Jack Tang, Raviraj Vankayala, Ben Lertsakdadet, Bernard Choi, John Stuart Nelson, and Bahman Anvari

ACS Appl. Mater. Interfaces, **Just Accepted Manuscript** • DOI: 10.1021/acsami.9b18624 • Publication Date (Web): 10 Dec 2019

Downloaded from pubs.acs.org on December 23, 2019

Just Accepted

“Just Accepted” manuscripts have been peer-reviewed and accepted for publication. They are posted online prior to technical editing, formatting for publication and author proofing. The American Chemical Society provides “Just Accepted” as a service to the research community to expedite the dissemination of scientific material as soon as possible after acceptance. “Just Accepted” manuscripts appear in full in PDF format accompanied by an HTML abstract. “Just Accepted” manuscripts have been fully peer reviewed, but should not be considered the official version of record. They are citable by the Digital Object Identifier (DOI®). “Just Accepted” is an optional service offered to authors. Therefore, the “Just Accepted” Web site may not include all articles that will be published in the journal. After a manuscript is technically edited and formatted, it will be removed from the “Just Accepted” Web site and published as an ASAP article. Note that technical editing may introduce minor changes to the manuscript text and/or graphics which could affect content, and all legal disclaimers and ethical guidelines that apply to the journal pertain. ACS cannot be held responsible for errors or consequences arising from the use of information contained in these “Just Accepted” manuscripts.

Intravital Vascular Phototheranostics and Real-Time Circulation Dynamics of Micro- and Nano-sized Erythrocyte-Derived Carriers

Wangcun Jia,[†] Joshua M. Burns,[#] Betty Villantay,[†] Jack C. Tang,[#] Raviraj Vankayala,[‡] Ben Lertsakdadet,^{†,‡} Bernard Choi,^{†,‡,∇} J. Stuart Nelson,^{†,‡} and Bahman Anvari^{#*}

[†]Beckman Laser Institute and Medical Clinic, Department of Surgery, University of California, Irvine, Irvine, CA, 92617

[#]Department of Bioengineering, University of California, Riverside, Riverside, CA, 92521

[‡]Radoptics LLC, Irvine, CA 92617

[‡]Department of Biomedical Engineering, University of California, Irvine, Irvine, CA, 92697

[∇]Edwards Life Sciences Center for Advanced Cardiovascular Technology, University of California, Irvine, Irvine, CA 92697

*e-mail: anvarib@ucr.edu

1
2
3 **ABSTRACT:** Erythrocyte-based carriers can serve as theranostic platforms for delivery of
4 imaging and therapeutic payloads. Engineering these carriers at micro- or nano-scales makes them
5 potentially useful for broad clinical applications ranging from vascular diseases to tumor
6 theranostics. Longevity of these carriers in circulation is important in delivering a sufficient
7 amount of their payloads to the target. We have investigated the circulation dynamics of micro
8 (~4.95 μm diameter) and nano (~91 nm diameter) erythrocyte-derived carriers in real time using
9 near-infrared fluorescence imaging, and evaluated the effectiveness of such carrier systems in
10 mediating photothermolysis of cutaneous vasculature in mice. Fluorescence emission half-lives of
11 micro- and nano-sized carriers in response to a single intravenous injection were ~49 and ~15
12 minutes, respectively. A single injection of micro-sized carriers resulted in threefold increase in
13 signal to noise ratio that remained nearly persistent over one hour of imaging time. Our results also
14 suggest that a second injection of the carriers seven days later can induce a transient inflammatory
15 response, as manifested by the apparent leakage of the carriers into the perivascular tissue. The
16 administration of the carriers into the mice vasculature reduced the threshold laser fluence to
17 induce photothermolysis of blood vessels from >65 to 20 J/cm². We discuss the importance of
18 membrane physicochemical and mechanical characteristics in engineering erythrocyte-derived
19 carriers, and considerations for their clinical translation.
20
21
22
23
24
25
26
27
28
29
30
31
32
33
34
35
36
37
38
39
40

41
42 **KEYWORDS:** cancer, erythrocyte engineering, delivery systems, laser dermatologic surgery,
43 near-infrared imaging, phototherapy, port wine stain
44
45
46
47
48
49
50
51
52
53
54
55
56
57
58
59
60

INTRODUCTION

Theranostic carrier systems offer a capability for delivery of imaging and therapeutic payloads to sites of interest. These delivery systems are often introduced into the body through vasculature. Carriers on a micro-size scale normally remain confined to the vasculature and, as such, can be useful for the imaging and treatment of vascular disease. Nano-sized carriers with dimensions <200 nm are relevant for the delivery of imaging and/or therapeutic agents to tumors since such carriers can extravasate out of the vasculatures and accumulate at tumor sites by the enhanced permeability and retention effect resulting from leaky tumor vasculature and impaired lymphatic drainage.¹

Various carrier systems such as polymeric particles,²⁻³ liposomes,⁴ genome-depleted bromo mosaic virus,⁵⁻⁶ and inorganic nanoplatfoms⁷ have been investigated.⁸ For conventional non-stealth particles, opsonin proteins present in the blood serum bind to the particles, resulting in recognition and removal of the particles by the reticuloendothelial system and shortening their blood circulation time.⁹ To address this issue, the surface of particles can be coated with polyethylene glycol (PEG).¹⁰ PEGylation can prolong systemic circulation time of the particles to a certain degree and increase their accumulation in a tumor site to enhance imaging or therapeutic efficacy. However, studies have shown that repeated administration of PEGylated particles results in accelerated blood clearance due to the production of anti-PEG antibodies.¹¹⁻¹² Moreover, dense and larger PEG chains hinder their interactions with the tumor microenvironment, inducing poor tumor penetration and uptake of particles.¹³ Therefore, researchers have been motivated to explore other materials as carrier systems for theranostic applications.¹⁴⁻¹⁵

Erythrocytes are under extensive investigation as carrier systems for the delivery of various payloads including pharmaceutical agents, imaging probes, and photo-activated materials.¹⁶⁻¹⁸ Key

1
2
3 advantages of erythrocyte-based delivery systems are attributed to their potential biocompatibility
4 and presence of specific membrane proteins, such as CD47 and decay-accelerating factor (CD55)
5 that can impede phagocytosis and prolong circulation.¹⁹ A particular feature of an erythrocyte-
6 derived delivery platform is that their diameter can be engineered from micro- to nano-scale based
7 on appropriate mechanical manipulation of erythrocytes, thereby providing a capability to develop
8 a versatile platform for broad biomedical and clinical applications.²⁰
9

10
11
12 A key issue pertaining to biomedical carrier systems, including those derived from erythrocytes,
13 is their longevity within the vasculature. In the context of vasculature imaging and photo-
14 therapeutics, the circulation lifetime of the carrier system determines the time window in which
15 the vasculature can be imaged with sufficient contrast, or irradiated with sufficient absorption. In
16 the context of cancer theranostics, increased circulation time of nano-carriers can result in greater
17 accumulation of the carriers within the tumors, which can enhance the efficacy of imaging or
18 therapy.²¹ While normal erythrocytes have circulation times on the order of 3-4 months, to the best
19 of our knowledge, real-time circulation dynamics of erythrocyte-derived optical carriers,
20 particularly as related to their diameters, have not been previously reported in the literature. Herein,
21 we report the first results on circulation dynamics of micro- and nano-sized erythrocyte-derived
22 optical carriers based on real-time fluorescence imaging of the particles within the sub-dermal
23 vasculature of healthy mice.
24
25

26
27 The erythrocyte-derived carriers in this study are doped with indocyanine green (ICG),
28 currently the only near-infrared (NIR) absorbing dye approved by the United States Food and Drug
29 Administration. ICG is an amphiphilic, water-soluble tricyanocyanine dye with a molecular mass
30 of 775 Da. Since tissue autofluorescence emission is dramatically reduced in NIR spectral band
31 (700-1700 nm), use of ICG can provide high signal-to-background ratio for biomedical imaging
32
33
34
35
36
37
38
39
40
41
42
43
44
45
46
47
48
49
50
51
52
53
54
55
56
57
58
59
60

1
2
3 applications. Another inherent advantage of ICG is that the NIR light used to excite ICG can
4
5 penetrate deeply into biological tissues (at least 1 cm depending on tissue type and wavelength) as
6
7 there is minimal photon absorption and scattering by endogenous molecules.²² Doping the
8
9 erythrocyte-derived particles with ICG serves two important purposes. First, ICG is used as an
10
11 optical tracer to fluorescently visualize the particles in real time. In doing so, time-dependent
12
13 recordings of ICG fluorescence signal provides pertinent information applicable to circulation
14
15 dynamics of erythrocyte-based delivery systems for various biomedical applications. Second, ICG
16
17 itself can endow the particles with phototheranostic capability so that these particles can be used
18
19 as materials for optical imaging and photo-therapeutic purposes.¹⁸ When activated by absorption
20
21 of an appropriate NIR wavelength, the particles can transduce the absorbed photon energy to emit
22
23 light (e.g., fluorescence emission) or generate heat^{18,23}, or mediate production of reactive oxygen
24
25 species.¹⁸ We refer to these optical particles as NIR erythrocyte-derived transducers (NETs) as
26
27 they can transduce the absorbed energy as described above. Another novel aspect of this study is
28
29 that for the first time, we demonstrate that in addition to their vascular fluorescence imaging
30
31 capability, NETs can also mediate photothermolysis of the vasculature in response to pulsed NIR
32
33 laser irradiation, particularly at lower light fluences when compared to laser irradiation of the
34
35 vasculature without exogenous chromophores. These results have relevance to the therapeutic
36
37 utility of NETs by mediating photothermolysis of cutaneous capillary malformations known as
38
39 port wine stains (PWSs).
40
41
42
43
44
45

46
47 Based on our in vivo real-time NIR fluorescence imaging results, we found that the average
48
49 emission half-life of micro-sized NETs (μ NETs, ~ 4.95 μ m diameter) in response to a single retro-
50
51 orbital injection was ~ 49 minutes, as compared to ~ 15 and 12 minutes for nano-sized NETs
52
53 (nNETs, ~ 91 nm diameter) and free ICG, respectively. μ NETs mediated threefold increase in
54
55
56
57
58
59
60

1
2
3 signal-to-noise ratio (SNR) for blood vessels that remained nearly persistent over the one hour of
4
5 imaging time post-injection. Furthermore, our imaging results suggest that the second injection of
6
7 μ NETs or nNETs seven days after the first injection induced a transient inflammatory response as
8
9 manifested by apparent vasodilation and vascular leakage of the contrast agent into the
10
11 perivascular tissue. We discuss the physicochemical and biomechanical factors that are related to
12
13 our findings. These factors are important for the engineering of a safe and effective erythrocyte-
14
15 derived carrier platform for clinical translation.
16
17
18
19

20 RESULTS

21
22
23 **Absorption, Fluorescence, and Diameter of NETs.** μ NETs and nNETs suspended in 310
24
25 mOsm phosphate buffered saline (PBS) showed dominant peaks at 803 and 802 nm (Figure 1a),
26
27 respectively, attributed to the monomeric form of ICG.²⁴ In comparison, the absorption spectrum
28
29 of 18 μ M free ICG dissolved in 310 mOsm PBS exhibited a dominant peak at 697 nm, which is
30
31 attributed to the H-like aggregate form of ICG.²⁴ In response to photo-excitation at 785 nm, the
32
33 fluorescence emission intensity values divided by the quantity of absorbed light (see Equation 1)
34
35 were higher for NETs than that for free ICG up to \sim 855 nm (Figure 1b). Encapsulation-enhanced
36
37 emission can be attributed to electrostatic interactions of amphipathic ICG molecules with NETs
38
39 constituents (e.g., phospholipids, proteins) which hinder the mobility of ICG, thus reducing non-
40
41 radiative relaxation from an excited electronic state. We have previously reported comprehensive
42
43 characterization studies related to physical and optical properties of μ NETs and nNETs.²⁴ These
44
45 properties included ICG concentration-dependent zeta potentials, absorption and emission spectra,
46
47 loading efficiency, excitation-emission maps, relative fluorescence quantum yield and
48
49 photostability, are not repeated here. As an example, we point out that the spectrally-integrated
50
51
52
53
54
55
56
57
58
59
60

fluorescence emissions of μ NETs, and nNETs formed by mechanical extrusion, are not altered in a statistically significant manner when stored at 4 or 37 °C for up to 12 hours.²⁴

The estimated mean peak hydrodynamic diameters of nNETs, as measured by dynamic light scattering (DLS), was \sim 91 nm ($n = 4$ measurements on each sample, Figure 1c). Lognormal fits to the DLS-based profiles yielded the mean peak \pm standard deviation (SD) diameters of 93 ± 1 nm. In Figure 1d, we present a representative confocal microscopy image of μ NETs. Based on the analysis of 30 μ NETs from this image, the estimated mean \pm SD diameters of μ NETs were 4.95 ± 0.63 μ m. The z-stack of the confocal images of μ NETS (Figure S1, Supporting Information) further demonstrates that ICG was localized in both the interior core and membrane shell of μ NETs.

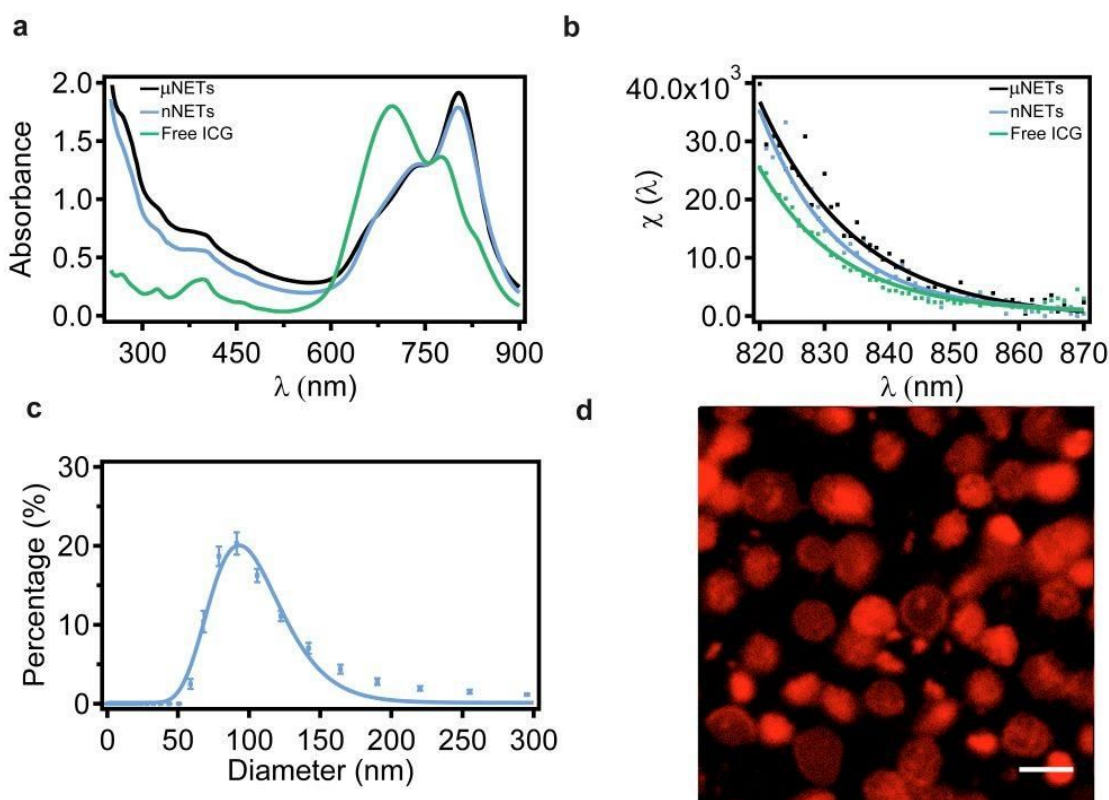
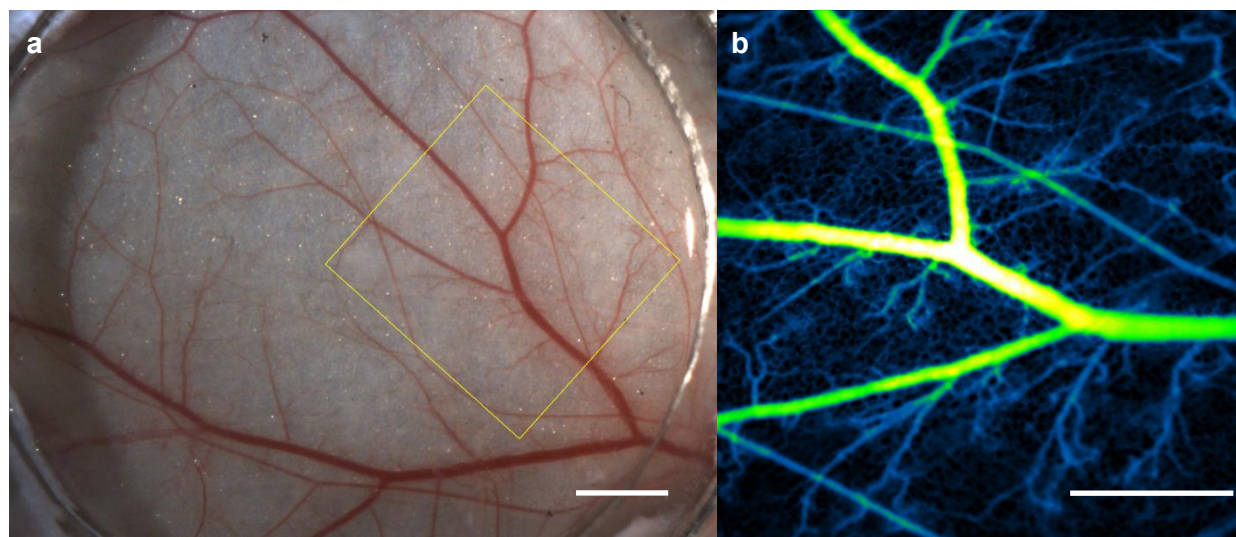


Figure 1. Characterization of NETs. (a) Absorption and (b) fluorescence emission intensity divided by the quantity of the absorbed light (see Equation 1) for μ NETs, nNETs and 18 μ M free ICG in 310 mOsm PBS and in response to 785 ± 2.5 nm excitation. (c) Hydrodynamic diameter distribution of nNETs suspended in 310 mOsm PBS as estimated by dynamic light scattering (DLS). The mean and standard deviation of the measurements ($n = 4$) are represented as circles and error bars, respectively. The estimated mean value of the peak diameter as determined from the lognormal fits (solid curves) is \sim 93 nm. (d) Fluorescence image

1
2
3 of μ NETs obtained by confocal microscopy. NIR emission is falsely colored in red. Scale bar corresponds
4 to 5 μ m. NETs were fabricated from bovine erythrocytes.
5
6

7 **Intravital fluorescence imaging of microvasculature using NETs as optical contrast agents.**

8
9 Co-registration of a photographic image of mouse dermal microvasculature within the window
10 chamber, obtained by white light illumination (Figure 2a), with a NIR fluorescence image
11 mediated by μ NETs (Figure 2b), demonstrates improved resolution to visualize both major and
12 minor blood vessels attained by using μ NETs. Dynamic angiography-like video in the first 37 s
13 after injection of μ NETs provides a clear presentation of the filling of μ NETs in the vasculature
14 (Video S1, Supporting Information). Representative dynamic changes in fluorescence intensity in
15 the vasculature over the 60 minutes imaging period after μ NETs injection is provided as Video
16 S2, Supporting Information. A corresponding montage of the same imaging sequence is presented
17 in Figure 2c.
18
19
20
21
22
23
24
25
26
27
28
29



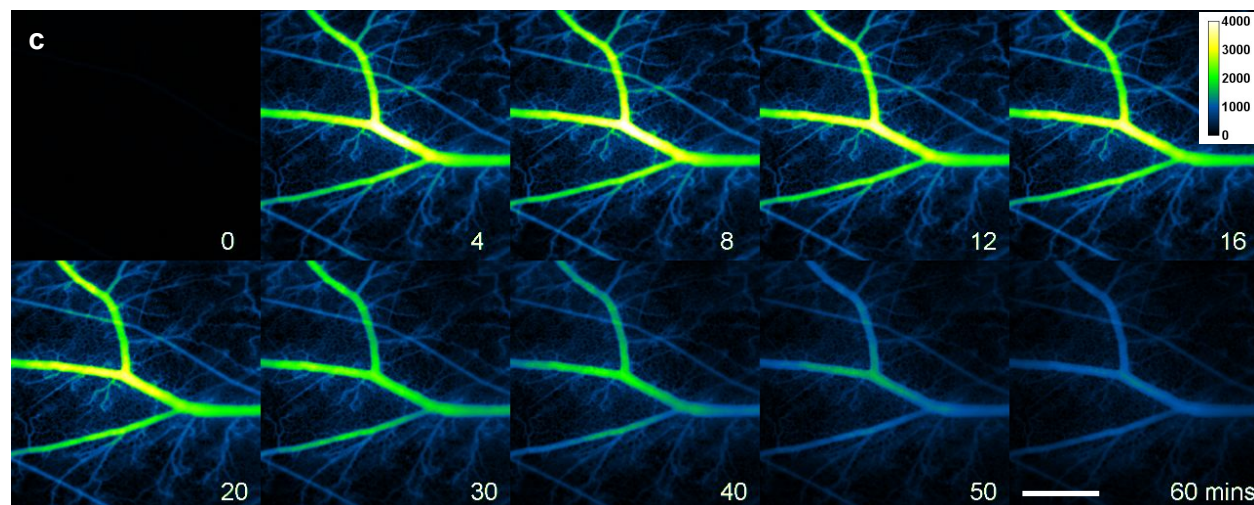


Figure 2. Intravital imaging of mouse skin microvasculature in window chamber. (a) Representative bright-field image and (b) its corresponding NIR fluorescent image at 6 minutes post μ NETs administration. (c) Montage demonstrating the dynamic changes in fluorescence intensity in the vasculature over the 60 minutes imaging period after μ NETs administration. White bars in Panels a, b and c represent 1 mm. White bar on the 60 mins panel applies to all images shown in Panel C. NIR images are falsely-colored. NETs were fabricated from bovine erythrocytes.

Intravital fluorescent images of blood vessels in the window chamber at different time points after μ NETs, nNETs, or free ICG administration are shown in Figure 3. The highest mean emission from blood vessels was observed at three minutes post injection for both μ NETs and nNETs (Figures 3a, d), and at 47 seconds for free ICG (Figure 3g) (the region of interests (ROI) for measuring fluorescence intensity are illustrated by the yellow outlines in Figure S2, Supporting Information). The difference in the peak fluorescence time could be related to the different transit times of μ NETs, nNETs and free ICG in arteries, veins, and capillaries. It also could be caused by the different elimination rates from the vasculature for the three agents. The maximum raw fluorescence intensity value for nNETs was significantly higher ($p < 0.05$) than those for μ NETs and free ICG (values of raw fluorescence intensity are provided in Figure S3, Supporting Information). At 30 minutes post-injection (Figures 3b, e), fluorescence intensity in the blood vessels was still high in response to either μ NETs or nNETs administration, but very low at the

1
2
3 same time after free ICG injection (Figure 3h). At 60 minutes post-injection (Figures 3c, f), blood
4
5 vessels could still be clearly visualized in response to both μ NETs and nNETs administration.
6
7 However, blood vessels injected with free ICG (Figure 3i) were barely distinguishable from the
8
9 background, thus confirming that free ICG was eliminated from the vasculature.
10
11
12
13
14
15
16
17
18
19
20
21
22
23
24
25
26
27
28
29
30
31
32
33
34
35
36
37
38
39
40
41
42
43
44
45
46
47
48
49
50
51
52
53
54
55
56
57
58
59
60

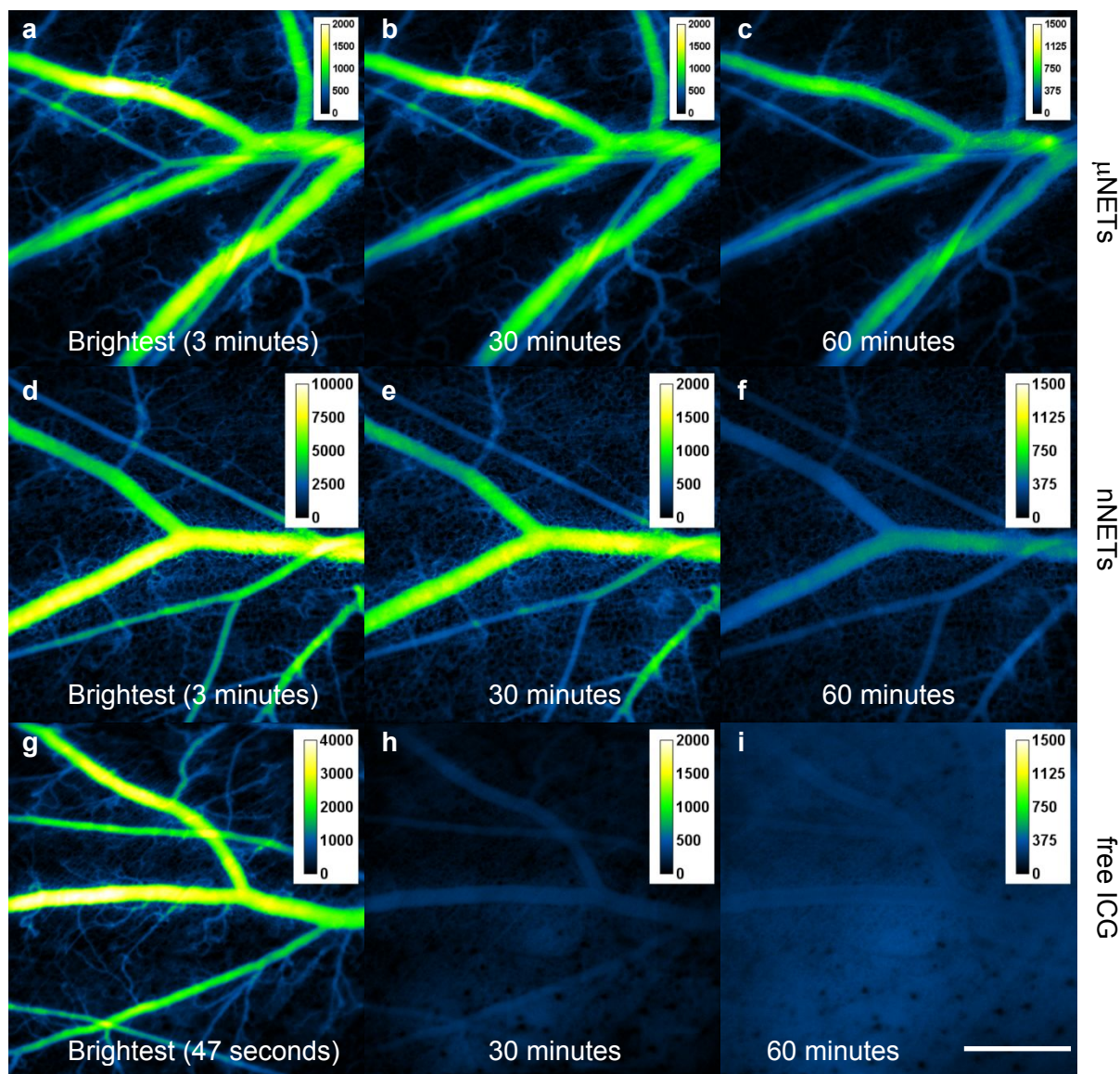


Figure 3. Intravital NIR fluorescent images of mouse skin microvasculature in the window chamber after single injection of NETs, or free ICG. (a-c) μ NETs, (d-f) nNETs, and (g-i) free ICG. Note that the scales in Panels a, d, g are different from each other. Panels a, d, and g correspond to the time at which the highest mean emission from blood vessels were observed for μ NETs, nNETs, and free ICG, respectively. White bar shown on panel i represents 1 mm, and applies to all images. NIR images are falsely-colored. NETs were fabricated from bovine erythrocytes.

In vivo emission dynamics and quantitative fluorescence analysis. Spatially-averaged emission intensities within the blood vessels (illustrated by yellow outlined ROIs in Figure S2, Supporting Information) from three animals were averaged first (Figure S4, Supporting Information). Normalized intensity values were calculated by dividing the raw fluorescence

intensities in each ROI by the maximum value in the corresponding ROI. Average normalized values from three animals for each agent indicated that μ NETs emission decayed more slowly as compared to those for nNETs and ICG (Figure 4a).

To obtain additional quantitative information from the fluorescent images associated with different agents, we determined the signal-to-noise ratio (SNR) between the blood vessels and the background noise in the perivascular tissue (see Equation 2). Mean SNR reached a maximum value of ~ 3 following injection of μ NETs and remained nearly persistent with only 18% reduction at one hour post injection (Figure 4b). Maximum values of SNR associated with nNETs and free ICG were similar (~ 3.2) and were reduced by 36 and 89%, respectively, at one hour post injection.

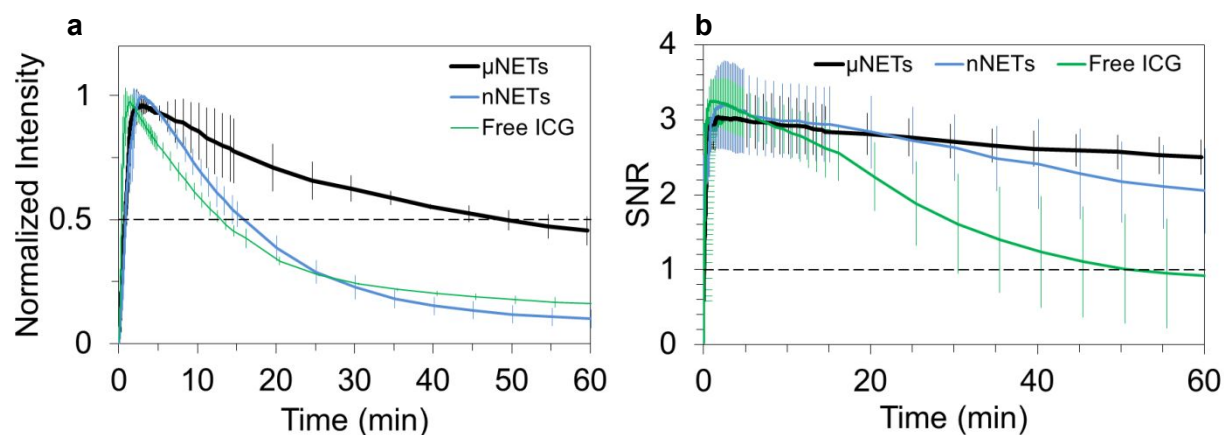
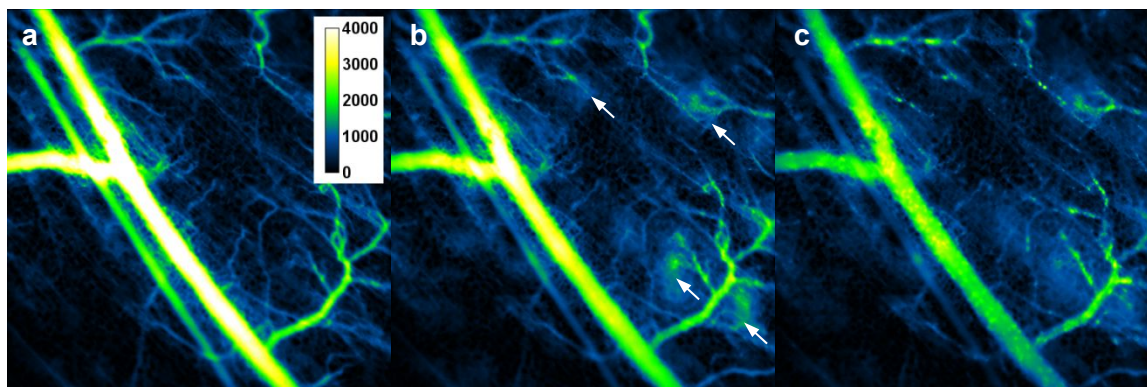


Figure 4. Quantitative fluorescence dynamics in response to a single injection of NETs or free ICG. Temporal characteristics of (a) normalized fluorescence intensity and (b) SNR (see Equation 2) in the blood vessels after single injection of NETs or free ICG. Each trace is the average of three experiments. Error bars represent the standard deviations from the mean values. NETs were fabricated from bovine erythrocytes.

The emission half-life was calculated as the time when the normalized fluorescence intensity value in the ROI was reduced from 1 to 0.5 (Figure 4a). Specifically, half-lives for μ NETs, nNETs, and ICG in the ROI were 49, 15, and 12 minutes, respectively. For μ NETs and nNETs, the normalized intensity could be fitted with exponential functions (Figure S5, Supporting Information) using either one-phase decay (Figures S5a,c) or two phase decay models with smaller residuals

(Figures S5b,d). However, for ICG, the normalized intensity curve could only be fitted with a two-phase decay model (Figure S5f, Supporting Information) but not a one-phase decay model (Figure S5e, Supporting Information). This difference implies that the elimination mechanisms for NETs or ICG are different.

In vivo emission dynamics of NETs in response to dual injection. Seven days after the first injection, we confirmed that there was no remaining fluorescence in the blood vessels, and administered a second injection of μ NETs or nNETs. While brightest emission was still observed at 3 minutes after the second injection of μ NETs (Figure 5a), some glowing spots around capillary tips appeared as early as 10 minutes (Video S3, Supporting Information), pointed by white arrows in Figures 5b, e, f. We also studied dual-injection of μ NETs fabricated from mice erythrocytes ($n=3$) in addition to those fabricated from bovine erythrocytes. Glowing spots around capillary tips were also observed after the second injection (Figure S6, Supporting Information). At later time points (30, and 60 minutes), bright stationary particles were observed in the main vessels and smaller vessels (Figures 5c-d). Besides stationary particles adherent to the vessel wall, there were also large particles flowing in the vessels that seemed to be aggregated μ NETs (Video S4, Supporting Information). These stationary and flowing large particles disappeared from the vasculature 24 hours after the second injection. All animals receiving dual injections recovered without any apparent problem.



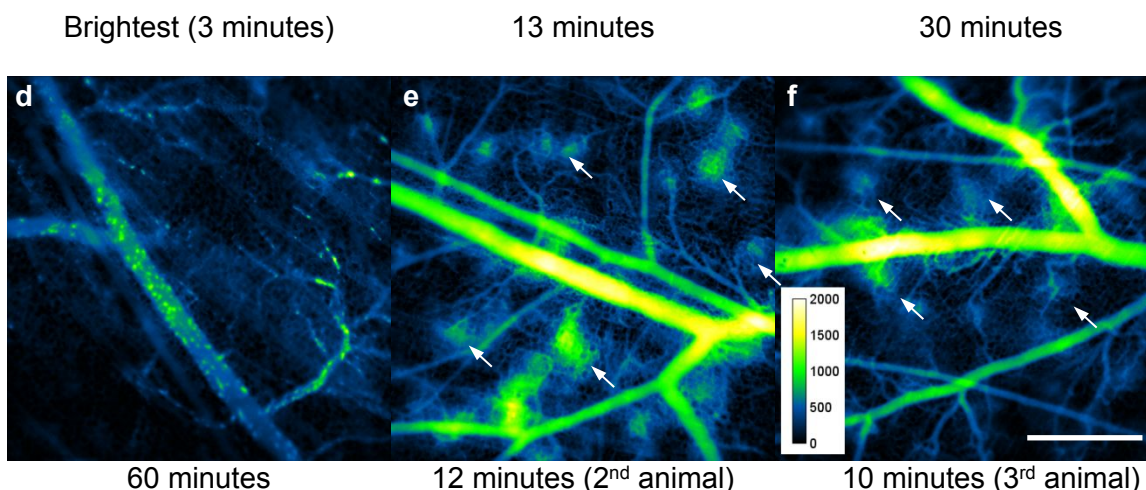


Figure 5. Intravital NIR fluorescent images of mouse skin microvasculature in the window chamber in response to second injection of μ NETs (7 days after first injection). (a-d) Fluorescent images acquired at 3, 13, 30, and 60 minutes for one mouse. (e-f) Fluorescent images at 12 and 10 minutes post-injection, respectively, for a second and third mouse. In Panels (b), (e) and (f), bright spots are visible in the regions around the tips of the capillaries (white arrows). In Panels (c) and (d), there are large and bright particles on the vessel wall. White bar represents 1 mm and applies to all panels. NIR images are falsely-colored. NETs were fabricated from bovine erythrocytes.

The average normalized fluorescence intensity (Figure 6a) associated with the second injection of μ NETs ($n=4$ animals) decayed more slowly as compared to those associated with the single injection of μ NETs (Figure 4a). The emission half-life in response to the second μ NETs injection was longer than one hour (Figure 6a). However, the presence of highly fluorescent aggregates adherent to the vessel walls (Figure 5d and Video S4) could skew the measured fluorescence intensity towards a slower decay rate and consequently a longer emission half-life. While the same maximum value of SNR (~ 3) was reached after the second injection of μ NETs, there was a more rapid decay in the SNR profile (Figure 6b). Reductions in SNR can be attributed to the presence of the glowing spots in the capillary regions (Figures 5e, f).

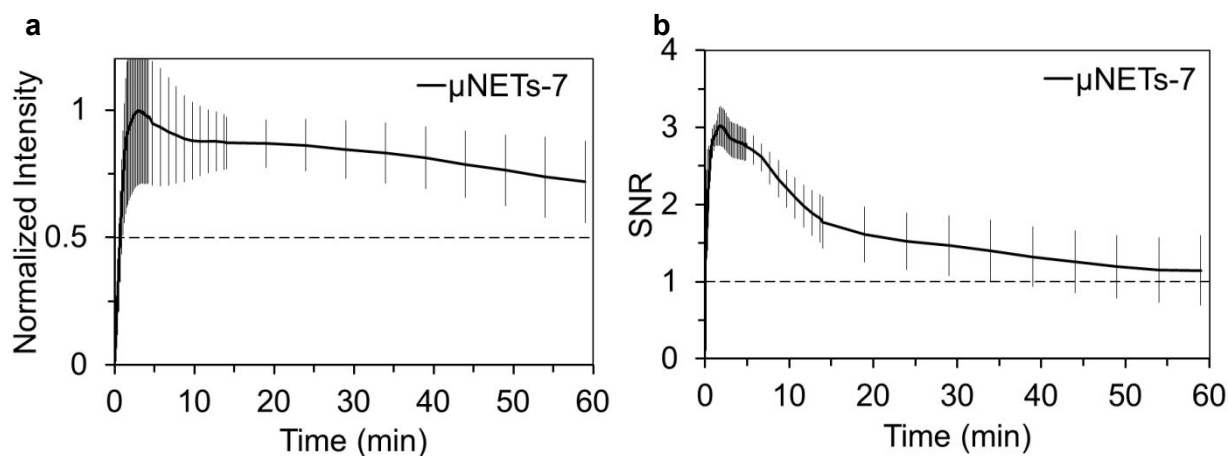


Figure 6. Quantitative fluorescence dynamics in response to the second injection of μ NETs (designated as μ NETs-7) seven days after the first injection. Temporal characteristics of (a) normalized fluorescence intensity and (b) SNR (see Equation 2) in the blood vessels after the second injection of μ NETs. Each trace is an average of four experiments. Error bars represent the standard deviations from the mean values. NETs were fabricated from bovine erythrocytes.

In response to the second injection of nNETs seven days after the initial injection, there was a progressive increase in background fluorescence (Figures 7a-c). Although, the fluorescence intensity in the ROIs was high, the image's SNR decayed substantially during the one hour time course after injection (Figure 7e). For the second injection of nNETs, the emission half-life was not consistent among the animals, ranging from 25 to >60 minutes (Figure 7d).

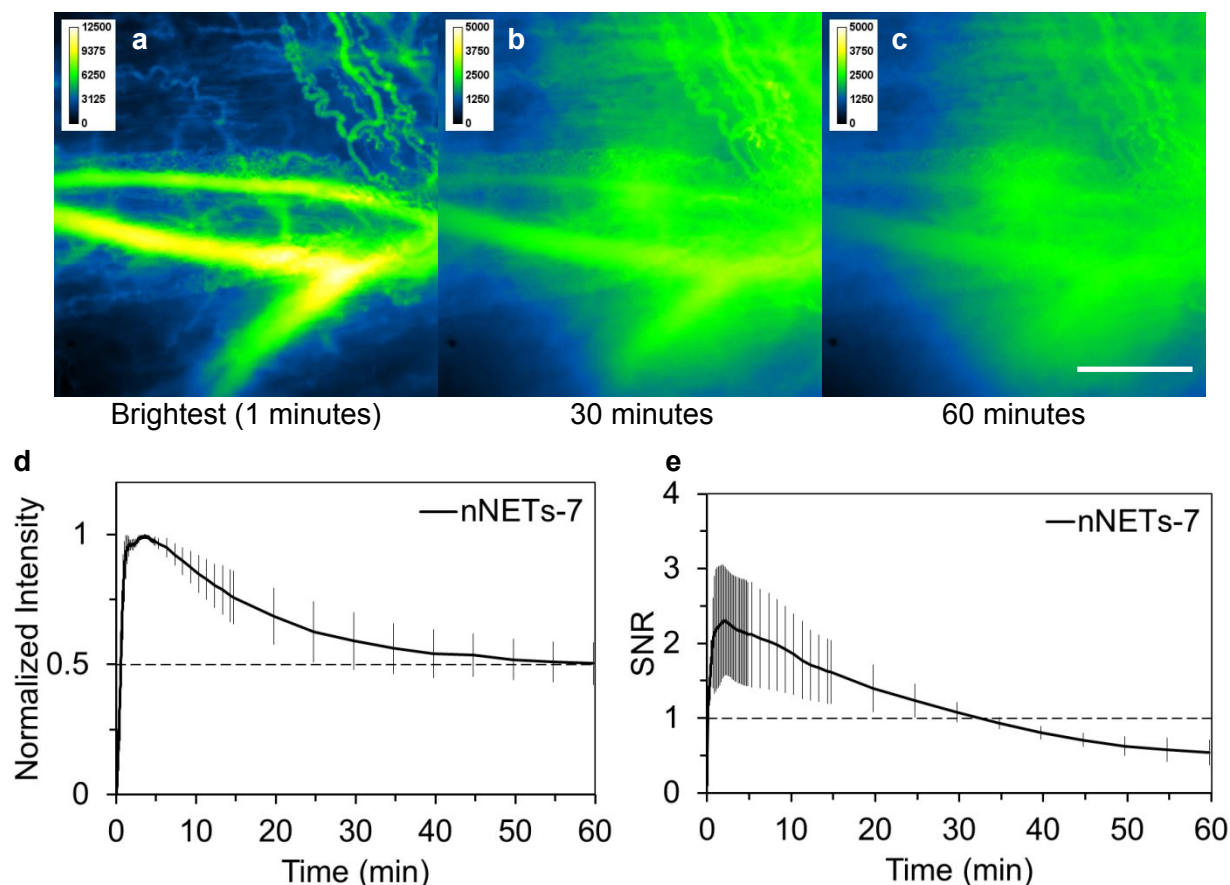


Figure 7. Intravital NIR fluorescent images of the microvasculature in the window chamber and quantitative fluorescence dynamics in response to second injection of nNETs (designated as nNETs-7). (a-c) Fluorescent images at one minute (time of maximum emission intensity), 30 and 60 minutes after second injection. Note that background tissue fluorescence intensity at 30 and 60 minutes after injection is quite high (Panels b, c). White bar in panel c represents 1 mm, and applies to all images. NIR images are falsely-colored. Temporal characteristics of (d) normalized fluorescence intensity and (e) SNR (see Equation 2) in the blood vessels after the second injection of nNETs. Each trace is the average of three experiments. Error bars represent the standard deviations from the mean values. NETs were fabricated from bovine erythrocytes.

We also studied dual injection of ICG or injection of NETs following ICG injection and vice versa (Table S1, Supporting Information). Emission dynamics of the second ICG injection was nearly the same as the first ICG injection. Emission dynamics of the μ NETs injection seven days following first ICG injection was similar to the first injection of μ NETs.

NETs-mediated photothermolysis of blood vessels in conjunction with pulsed NIR laser irradiation. We investigated the effectiveness of μ NETs in mediating photothermolysis of the microvasculature using laser speckle contrast (LSC) imaging, which characterizes blood flow dynamics.²⁵ Without any exogenous agents, 755 nm pulsed laser irradiation (3 ms, 10 mm spot size) at a fluence as high as 65 J/cm² was insufficient to induce photothermolysis of all the irradiated blood vessels (Figures 8a, c). Following retro-orbital administration of μ NETS, blood vessels were irradiated at 100 s after injection, the time at which peak fluorescence intensity was approximately achieved. When the fluence was 20 J/cm², photothermolysis of most blood vessels occurred (Figures 8b, e). Fluence of 30 J/cm² was sufficient to induce photothermolysis of all the irradiated blood vessels (Figures 8c, f).

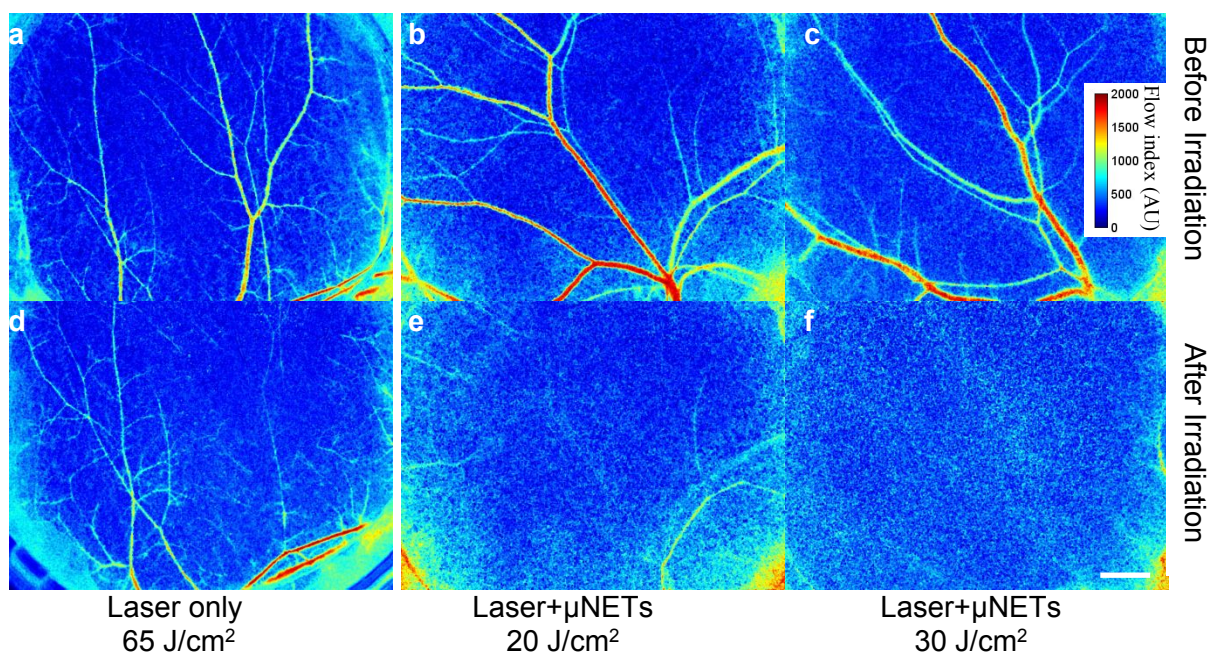


Figure 8. Blood flow maps of skin microvasculature within the window chamber obtained by laser speckle contrast (LSC) imaging. (a-c) Before, and (d-f) ~5 minutes after 755 nm laser irradiation at various fluences without (d) or with (e, f) administration of μ NETS. Laser pulse duration and spot size were 3 ms, and 10 mm, respectively. White bar represents 1 mm and applies to all images. Images are falsely-colored. NETS were fabricated from bovine erythrocytes.

DISCUSSION

Encapsulation of imaging or therapeutic payloads into erythrocyte-derived carrier systems has gained increasing attention.^{16, 18-19} An important consideration in relation to these carriers is their longevity within the vasculature as it has relevance to the bioavailability of the encapsulated cargo for an intended clinical application. In this study, we investigated the vascular longevity of erythrocyte-derived carriers by real time fluorescence imaging, and utilized quantitative metrics (SNR) to assess the in vivo imaging capability of the carriers as a function of their diameters. We have also demonstrated the effectiveness of these carriers when doped with ICG in mediating photothermolysis of blood vessels. We discuss inter-related factors that can provide the mechanistic basis for our observations and guide further design and development of these particles for clinical translation. We also discuss the relevance of these particles to laser treatment of cutaneous capillary malformations.

Membrane physicochemical characteristics and role of phosphatidylserine in clearance of NETs. The membrane bilayer of normal red blood cells (RBCs) is composed of phospholipids, cholesterol and an array of transmembrane proteins involved in transport, adhesion and signaling, as well as those defining the various blood group antigens.²⁶ Similar to other eukaryotic cells, the four major phospholipids of RBCs lipid bilayer are asymmetrically distributed where phosphatidylcholine and sphingomyelin are predominantly confined in the outer leaflet, whereas phosphatidylethanolamine and anionic phosphatidylserine (PS) are located in the inner leaflet. Localization of PS in the inner leaflet of normal RBCs is achieved by an ATP-dependent aminophospholipid translocase (flippase) that can rapidly shuttle PS from outer to inner leaflet. This activity is dependent on intracellular concentration of Ca^{+2} , and presumably associated with a P-type Mg^{2+} -ATPase²⁷ with ATP11C identified as a flippase.²⁸ Redistribution of PS to the

external leaflet is considered as a hallmark of RBCs undergoing apoptosis, and their phagocytosis by macrophages, which contain PS receptors that recognize surface-exposed PS on apoptotic RBCs.²⁹⁻³¹ Furthermore, PS surface exposure is associated with removal of senescent normal RBCs by spleen macrophages.³²⁻³³

Our results indicate that the fractions of PS-positive, micro-sized erythrocyte ghosts (μ EGs) and nano-sized EGs (nEGs) were comparable, and significantly higher than that for RBCs (Figure 9). This result suggests that display of PS on the outer leaflet can be induced by hypotonic treatment of RBCs,³⁴ and before the subsequent mechanical extrusion of hemoglobin-depleted μ EGs to form nEGs. NETs with surface-exposed PS can then be recognized and engulfed by macrophages and, subsequently, removed from the vasculature.

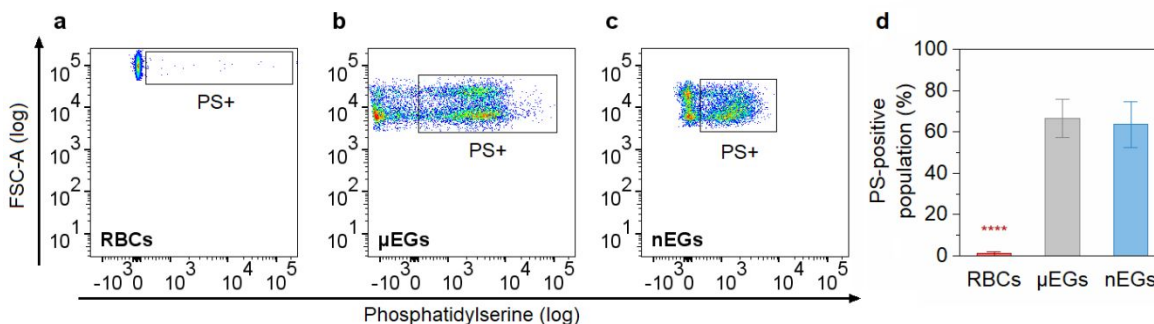


Figure 9. PS quantification for RBCs, μ EGs, and nEGs as determined by flow cytometry. (a-c) Representative dot plots of forward scattering vs. fluorescence emission of Alexa Fluor 488-labeled annexin V to target PS on RBCs, μ EGs, and nEGs. Boxed regions correspond to PS-positive RBCs and EGs. (d) Mean fraction of PS-positive RBCs, μ EGs, and nEGs populations. Error bars represent one standard deviation from the mean ($n=3$ samples for each indicated material). **** indicates statistically difference ($p < 0.0001$) between the mean value for RBCs vs those for μ EGs and nEGs. Note that some fraction of nEGs may have been too small to be detected and do not appear on the dot plot.

In response to a single injection, nNETs have a lower average half-life in blood (~ 15 min) as compared to μ NETs (~ 49 min) (Figures 4a, b). Since nearly the same fractions of μ NETs and nNETs were PS-positive, the shorter half-life of nNETs in blood suggests that the removal rate of nNETs from the vasculature by macrophages is more efficient than the removal rate of μ NETs. Given that the mean peak diameter of nNETs (~ 91 nm) is smaller than the average width of splenic

1
2
3 interendothelial slits (~650 nm).³⁵ they can gain re-entry into the circulatory system; however, they
4
5 can also be recognized by splenic macrophages within the cords of the red pulp (e.g., due to PS
6
7 surface exposure), and subsequently removed from circulation. The shorter emission half-life of
8
9 nNETs suggests that they may be more efficiently moved out of circulation by the spleen. The rate
10
11 of a single phagocytosis event has been shown to be faster for engulfment of smaller particles,
12
13 whereas large or irregularly shaped particles, such as μ NETs, may be phagocytosed at a slower
14
15 rate.³⁶ In a recent study of biodistribution of NETs in healthy Swiss Webster mice, we found that
16
17 a statistically significant ($p < 0.05$) higher level of nNETs (~26% of the injected amount per organ
18
19 mass) were in mice spleens extracted 6 hours post injection, as compared to ~19% for μ NETs.³⁷
20
21
22
23

24 Both nNETs and μ NETs with surface-exposed PS can also be recognized by Kupffer cells,
25
26 macrophages adherent to the endothelial lining of liver sinusoids. Remaining nNETs escaping the
27
28 liver Kupffer cells can then pass through the pores (~170 nm diameter³⁸) between the fenestrated
29
30 endothelial lining in liver sinusoids, extravasate into the space of Disse, and be eliminated from
31
32 the body through the hepatobiliary mechanism, as mediated by hepatocytic uptake and subsequent
33
34 secretion into the bile ducts.
35
36

37 While the mechanisms of NETs removal by macrophages remain to be fully understood, several
38
39 factors influence the rate of the phagocytic activity induced by μ NETs and nNETs. These factors
40
41 include variations between the surface physicochemical characteristics of μ NETs vs. nNETs such
42
43 as differences in PS surface distribution, including the degree of PS spatial heterogeneities and
44
45 surface density of exposed PS; differences in the presence and/or conformation of phagocytic
46
47 impeding glycoproteins induced during fabrication (e.g., by mechanical extrusion to form nNETs)
48
49 or possibly resulting from the greater surface curvature of nNETs; and differences in opsonization
50
51 of μ NETs and nNETs in terms of the conformation of the opsonized proteins on the surface of
52
53
54
55
56
57
58
59
60

1
2
3 NETs due to surface curvature variations. One PS-binding opsonin is lactadherin (milk fat globule
4 epidermal growth factor 8), a glycoprotein secreted by activated macrophages,³⁹ that binds to $\alpha_v\beta_3$
5 and $\alpha_v\beta_5$ integrins on macrophages and epithelial cells, respectively.⁴⁰⁻⁴¹ Lactadherin opsonization
6 is also known to be size-dependent,⁴² which may contribute to the difference between emission
7 half-lives of NETs and nNETs.
8
9

10
11
12
13
14
15 Increased longevity of μ NETs in blood vessels may be a resultant of their more effective
16 localization to the vessel walls as compared to nNETs. It has been reported that particles with
17 diameters < 100 nm move with RBCs in the mainstream of the blood vessel lumen whereas larger
18 particles (~ 1 μ m diameter) tend to preferentially localize near the wall.⁴³ In another study, hydrogel
19 particles with diameter of ~ 2 μ m had enhanced margination to the wall when compared to particles
20 with 500 nm diameters.⁴⁴ Hence, nNETs may move with RBCs in the mainstream of the vessel
21 lumen whereas μ NETs may be located in close proximity to the endothelial cells, giving rise to
22 increased longevity in the blood vessels and subsequently increased emission half-life.
23
24
25
26
27
28
29
30
31
32

33
34 The mechanisms underlying our observations with the second injection of NETs may be related
35 to some type of induced “priming” effects in response to the first injection. One observation was
36 the presence of bright stationary spots on the vessel wall (Figures 5c-d, Video S4, Supporting
37 Information) and glowing regions around the capillary tips (Figures 5b, e, f, Video S3, Supporting
38 Information) after the second injection of μ NETs. RBCs (and potentially NETs) with surface-
39 exposed PS can bind to PS receptors on the endothelial cells of the vasculature.⁴⁵⁻⁴⁶ These receptors
40 include $\alpha_v\beta_3$ integrins and CD36,⁴⁷ and CXCL16,⁴⁸ a chemokine that can also be present as a
41 transmembrane protein to act as a scavenger receptor and bind to PS. It has been demonstrated that
42 both the PS receptor mRNA and the receptor levels in endothelial cells reach their respective
43 maximum values at 4 and 6 hours in response to interleukin (IL)-1 α induced activation in vitro.⁴⁶
44
45
46
47
48
49
50
51
52
53
54
55
56
57
58
59
60

1
2
3 Binding of PS-exposed RBCs to the endothelial PS receptor has also been reported as a basis for
4 the adhesion of RBCs to the endothelium of the central retinal vein.⁴⁹ Lactadherin-mediated
5 phagocytosis of PS-exposed RBCs by endothelial cells through the α_v integrin pathway has been
6 indicated.⁵⁰
7
8
9
10

11
12 After the first injection of NETs, the endothelial cells may be primed in a way to interact more
13 effectively with the PS on the surface of the second-injected NETs through the activated PS
14 receptors. Although it is not known if the first injection of NETs with PS surface exposure can
15 induce up-regulation of the PS receptor mRNA and expression of the receptor on endothelial cells,
16 it may represent a priming effect, leading to binding of the NETs to endothelial cells upon the
17 second injection which is manifested by the adherent fluorescent particles to the vessel wall and
18 the glowing regions around the capillary tips. Other types of priming effects resulting from the
19 first injection of NETs may lead to the production of cytokines, including tumor necrosis factor
20 (TNF)- α by macrophages, and activation of the complement system such as the production of C3a
21 and C5a fragments to cause dilation of small blood vessels after the second injection of NETs.
22 Such dilated small vessels could accommodate the μ NETs, a mechanism consistent with the
23 observed glows from the capillary regions in Figures 5b, e, f. The priming responses may also
24 represent a sensitization effect that involves the production of immunoglobulin E (IgE) after the
25 first injection of NETs. The second injection may subsequently trigger the activation of IgE
26 binding cells, such as basophils and mast cells.
27
28
29
30
31
32
33
34
35
36
37
38
39
40
41
42
43
44
45
46

47 Another observation was the increase in fluorescence emission from perivascular areas after the
48 second injection of nNETs (Figures 7b, c). These results seem to suggest that there was
49 extravasation of nNETs from the microvasculature after its second injection. Increased
50 permeability of blood vessels, leading to vascular leakage, is associated with an inflammatory
51
52
53
54
55
56
57
58
59
60

1
2
3 response and may have been induced by a priming effect after the first injection of nNETs.
4
5 Cytokines, such as TNF- α , IL1, and IL6, released during inflammation act on endothelial cells,
6
7 leading to increased vascular permeability.⁵¹ Vascular endothelial growth factor (VEGF) is also a
8
9 contributor to increased vascular permeability by uncoupling endothelial cell-cell junctions and
10
11 inducing endothelial fenestrations.⁵²⁻⁵³ Several growth factors, including epidermal growth factor
12
13 and transforming growth factor- α can upregulate VEGF mRNA expression. Additionally,
14
15 inflammatory cytokines, such as IL1- α and IL-6, can induce the expression of VEGF in various
16
17 cell types.⁵⁴
18
19
20
21

22 The integrity of endothelial cell-cell junction is regulated by the adherens, tight, and gap
23
24 junctions comprised of different adhesion molecules.⁵⁵ At adherens junctions, the VEGFR2
25
26 receptor associates with vascular endothelial (VE)-cadherin to regulate the cell-cell junction
27
28 integrity and provide a mechanism for VEGF-mediated vascular disruption.⁵² It has been
29
30 demonstrated that Src family protein tyrosine kinases are required for VEGF-induced
31
32 phosphorylation of adherens junctions proteins, which leads to vascular leakage in vivo.⁵² Once
33
34 these paracellular pathways have become leaky, nNETs with diameters on the order of ~ 91 nm
35
36 can extravasate out of the vasculature through the induced endothelial gaps as compared to μ NETs
37
38 with substantially larger diameters (~ 4.95 μ m diameter). Leakage of negatively-charged
39
40 mecaptoundeonic acid-capped silver nanoparticles after a single injection⁵⁶ and titanium dioxide
41
42 nanoparticles following repeated injections in mice have been reported.⁵⁷
43
44
45
46

47 **Biomechanical characteristics.** Normal RBCs are highly deformable structures. The discoid
48
49 biconcave shape of normal RBCs endows them with a high surface-to-volume ratio (~ 1.5) and
50
51 facilitates remarkable reversible deformations that allows their repeated passages through narrow
52
53 capillaries as they transverse from the splenic cord to splenic sinus without significant changes in
54
55
56
57
58
59
60

1
2
3 their surface area. The excess surface area (~40% higher than a sphere of the same volume),
4
5 coupled with the structural organization of normal RBCs, are the key determinants of the
6
7 mechanical characteristics of RBCs. The strong adhesion between the membrane bilayer and the
8
9 cytoskeleton is essential in maintaining the membrane surface area. This adhesion is provided by
10
11 the linkages between the intracellular domains of membrane proteins and spectrin-based
12
13 cytoskeleton network.²⁶ Particularly important linkages are provided by membrane proteins Band
14
15 3 and RhAG that link to the spectrin network via Ankyrin, and glycophorin C, XK, Rh, and Duffy,
16
17 which provide the linkage via protein 4.1R.⁵⁸⁻⁵⁹ Binding of PS to cytoskeletal proteins and the
18
19 spectrin network is also an important contributor to the mechanical stability and deformability of
20
21 normal RBCs.⁶⁰⁻⁶¹
22
23
24
25

26 Rupturing the PS linkages to cytoskeletal proteins, in addition to structural changes in the
27
28 spectrin network, may occur during the mechanical extrusion steps when fabricating the nNETs.
29
30 It is possible that such physical changes to the architecture of nNETs may alter their mechanical
31
32 properties. However, in comparison to PS surface exposure as a mechanism for removal of nNETs
33
34 from the vasculature, the mechanical characteristics of nNETs may not play a major role in their
35
36 circulation dynamics since nNETs are sufficiently small to pass through splenic interendothelial
37
38 slits and be re-introduced into circulation (if escaping the splenic macrophage cells).
39
40
41

42 For μ NETs, their mechanical properties and induced sphericity can play an impactful role in
43
44 influencing their circulation dynamics. Loss of membrane surface area and the resulting shape
45
46 change from discoids to spheres compromises the ability of μ NETs to effectively transverse
47
48 through the splenic slits so that they may become trapped within the cords and phagocytosed by
49
50 macrophages.⁶² The resultant shape change of μ NETs also implies that structural changes to the
51
52 spectrin network as well as membrane-cytoskeletal adhesion could occur which ultimately affect
53
54
55
56
57
58
59
60

1
2
3 the mechanical characteristics of μ NETs. In a recent study, we reported that the membrane
4 stiffness of μ NETs is higher than that of RBCs by about 28%-62%,⁶³ therefore, indicating a
5
6 reduction in deformation capability of μ NETs for effective splenic passage.
7
8
9

10 While the depletion of hemoglobin from RBCs during the formation of μ NETs can contribute
11 to the resulting shape changes, the ensuing mechanical changes are likely not a contributing factor
12 in influencing the longevity of μ NETs in circulation as compared to PS-mediated removal that
13 results from the hypotonic treatment of RBCs. Cytoplasmic viscosity of RBCs increases with
14 increased levels of intracellular hemoglobin concentration,⁶⁴⁻⁶⁵ hence, reducing the deformation
15 capability of RBCs. However, in the case of μ NETs, a reduction in cytoplasmic viscosity is actually
16 expected due to hemoglobin depletion.
17
18
19
20
21
22
23
24
25

26 The various factors described above, including PS surface exposure, changes in shape, lowered
27 surface-to-volume ratio, reduced deformability and increased membrane stiffness, can possibly
28 induce prothrombotic effects by NETs. In particular, in response to the second injection of μ NETs,
29 we observed bright particles flowing in the vessels that appeared to be aggregated (Video S4,
30 Supporting Information). These aggregates may be a composite of μ NETs and platelets. Formation
31 of μ NETs aggregates is consistent with the reported formation of stacked rouleaux of RBCs.⁶⁶
32 While the mechanisms of RBC rouleaux formation is not fully understood, proposed mechanisms
33 that may also be relevant to NETs, including the role of specific plasma proteins (particularly
34 fibrinogen) adsorbed on adjacent RBCs to mediate bridging of the RBCs,⁶⁷ or conversely, a lower
35 localized protein concentration near the surface of RBCs (as compared to the surrounding medium),
36 leading to an osmotic gradient and attractive forces.⁶⁸ Since the formation of RBCs rouleaux is
37 reversible as the shear rate increases, it is also possible that a similar reversible process takes place
38
39
40
41
42
43
44
45
46
47
48
49
50
51
52
53
54
55
56
57
58
59
60

1
2
3 with μ NETs aggregates. In the course of our study, the observed μ NETs aggregates disappeared
4
5 within 24 hours after injection.
6

7
8 In relation to toxicological assessment of NETs, results of our recent study in Swiss Webster
9
10 mice indicated that values of various hematological profiles (including white blood cell count,
11
12 RBC count, platelets, hemoglobin, and hematocrit) at 24 hours post-injection of μ NETs or nNETs
13
14 were either within the normal range or not changed in a statistically significant manner.³⁷ Similarly,
15
16 there were no statistically significant changes in levels of alanine aminotransferase and aspartate
17
18 aminotransferase, enzymes associated with liver function, or any changes in levels of urea nitrogen
19
20 and creatinine associated with kidney function. Furthermore, histological analysis of various
21
22 organs (heart, liver, spleen, lung, and kidney) did not show any pathological alterations.
23
24
25

26 **Example of clinical application and outlook.** A particular application of μ NETs relates to
27
28 laser treatment of port wine stain (PWS) birthmarks. PWSs are currently treated by laser irradiation
29
30 using visible wavelengths in the range of 585-595 nm which are preferentially absorbed by
31
32 hemoglobin, an endogenous chromophore in blood. Conversion of the absorbed light to heat causes
33
34 thermal damage to the blood vessels and subsequent PWS clearance. However, melanin within the
35
36 melanocytes, located in the basal epidermal layer of skin and residing over the abnormal plexus of
37
38 dermal capillaries, has a relatively strong optical absorption over the current laser treatment
39
40 spectral band. As such, photons intended to reach the dermal vasculature are partially absorbed
41
42 within the epidermis. The outcome can be non-specific thermal injury to the epidermis and
43
44 insufficient heat generation within the vasculature to provide an adequate treatment.
45
46
47
48

49 An alternative phototherapeutic approach can potentially be developed by using NIR
50
51 wavelengths in conjunction with intravascular administration of μ NETs. For example, by changing
52
53 the treatment wavelength from 585 to 755 nm, a nearly threefold reduction in the absorption
54
55
56
57
58
59
60

1
2
3 coefficient of a single melanosome can be achieved.⁶⁹ This approach offers several advantages:
4
5 (1) reduced risk of non-specific thermal injury to the epidermis to potentially allow treatment of
6
7 individuals with moderate to heavy pigmentation;⁷⁰ (2) increased depth of optical penetration to
8
9 reach deeply-seated blood vessels (e.g., > 500 μm below the skin surface);⁷⁰ and (3) heat
10
11 generation within the blood vessels resulting from the absorption of ICG within μNETs to induce
12
13 photothermolysis of the abnormal vasculature plexus. Our results demonstrate that by
14
15 encapsulating ICG within μNETs , its retention time within the vasculature is prolonged (~12
16
17 minutes half-life for free ICG vs ~49 minutes for μNETs). Therefore, μNETs can potentially
18
19 extend the therapeutic window of time during which laser therapy of PWS can be performed, as
20
21 compared to free ICG.
22
23
24
25

26
27 In consideration of the aforementioned physicochemical and biomechanical factors associated
28
29 with NETs, it is important that these factors are taken into account during the fabrication process
30
31 of erythrocyte-derived carriers with the aim of not only prolonging the retention time of the
32
33 particles within the vasculature but also overcoming potentially adverse effects. As suggested by
34
35 our imaging results, the second injection of erythrocyte-derived carriers after one week following
36
37 the first injection can lead to an inflammatory response. Therefore, adequate injection interval
38
39 protocols, as well as fabrication protocols, need to be developed to avoid undesirable inflammatory
40
41 responses.
42
43
44

45 46 **CONCLUSION**

47
48 We have investigated the circulation dynamics of micron and nano-sized erythrocyte-derived
49
50 carriers in real time by near infrared fluorescence imaging of mice vasculature. The average
51
52 emission half-lives of micro- and nano-sized carriers in blood vessels in response to a single
53
54 intravenous injection were ~49 and 15 minutes, respectively. Second injection of the particles
55
56
57
58

1
2
3 seven days after the first injection increased the average emission half-life to > 1 hour for micro-
4 sized, with variable half-life ranging from ~25 minutes to >60 minutes for nano-sized carriers.
5
6 Surface exposure of phosphatidylserine on the surface of these carriers can be an important
7
8 mechanism for their removal from circulation. The shorter emission half-life of the nano-sized
9
10 particles in blood after the first injection suggests that macrophages may be more efficient in
11
12 removal of these particles when mediated through a phosphatidylserine surface exposure
13
14 mechanism. Shape and deformation characteristics of micro-sized carriers can also contribute to
15
16 the circulation time of these particles. Such biochemical and biomechanical characteristics are
17
18 important considerations towards the engineering of erythrocyte-derived platforms for clinical
19
20 translation in a safe and effective manner.
21
22
23
24
25
26

27 **MATERIALS AND METHODS**

28
29
30 **Fabrication of NETs.** Erythrocytes were separated from bovine whole blood (Rockland
31
32 Immunochemicals, Inc., Limerick, PA) by centrifugation (1,300xg, 5 minutes, 4 °C) and the
33
34 plasma and buffy coat were discarded. Isolated erythrocytes were washed twice with 310 mOsm
35
36 phosphate buffer saline (PBS) (referred to as the 1X solution) (pH ~8.0), and then subjected to
37
38 hypotonic treatment using 0.25X PBS (80 mOsm, pH ~8.0) and centrifuged (20,000xg, 15 minutes,
39
40 4 °C). This process was repeated until an opaque pellet containing micro-sized hemoglobin-
41
42 depleted erythrocyte ghosts (EGs) was formed. To obtain nano-sized EGs (nEGs), the micro-sized
43
44 EGs (μ EGs) were extruded 40 times through 400 nm polycarbonate porous membranes (Track-
45
46 Etched Membranes, Whatman, Florham Park, NY), followed by 40 more extrusions through 200
47
48 nm polycarbonate membranes, and another 40 times through 100 nm polycarbonate membranes
49
50 using an Avanti mini extruder (Avanti Polar Lipids, Inc., Alabaster, AL).
51
52
53
54
55
56
57
58
59
60

We concentrated the μ EGs and nEGs 10 times by centrifugation (20,000xg, 15 minutes, 4 °C for μ NETs; 98,800xg, 1 hour, 4 °C for nNETs) and re-suspended the EGs pellet in 1 ml of 1X PBS. To form μ NETs or nNETs, 1 ml of concentrated μ EGs or nEGs were incubated in loading buffer consisting of 3 ml of 2.58 mM free ICG dissolved in water and 3 ml of hypotonic buffer ($\text{Na}_2\text{HPO}_4/\text{Na}_2\text{H}_2\text{PO}_4$, 140 mOsm, pH \sim 5.8) for 10 minutes (final ICG concentration in loading buffer \sim 1.11 mM). After incubation, the resulting NETs suspensions were centrifuged (20,000xg, 15 minutes, 4 °C for μ NETs; 74,000xg, 30 minutes, 4 °C for nNETs) and supernatants were removed. The pellets were washed two more times using 1X PBS to remove any remaining non-encapsulated ICG, and the final μ NETs and nNETs were suspended in 1X PBS and stored at 4°C in the dark.

Characterization of NETs. Absorption spectra of NETs and 18 μM free ICG suspended in 1X PBS were obtained using a UV-visible spectrophotometer (Cary 50 UV-Vis spectrophotometer, Agilent Technologies, Santa Clara, CA) with an optical path length of 1 cm. To avoid saturation in measurements of NIR absorbance values during spectral recordings, solutions of μ NETs and nNETs were further diluted by a factor of 100 using 1X PBS.

Fluorescence emission spectra of NETs and 6.5 μM free ICG in 1X PBS were acquired in response to 785 ± 2.5 nm excitation with a 450W xenon lamp and recorded over the 820 - 870 nm spectral band using a fluorimeter (Fluorolog-3 spectrofluorometer, Edison, NJ). Fluorescence emission spectra (χ) scaled to the quantity of the absorbed light were determined as:

$$\chi(\lambda) = \frac{F(\lambda)}{1 - 10^{-A(\lambda_{\text{ex}})}} \quad (1)$$

where A and F are the wavelength (λ) dependent absorbance and intensity of the emitted fluorescence light, respectively, and λ_{ex} is the excitation wavelength. Hydrodynamic diameters of

1
2
3 NETs suspended in 310 mOsm PBS was measured by dynamic light scattering (Zetasizer
4 NanoZS90, Malvern Instruments Ltd, Malvern, United Kingdom).
5
6

7
8 **Confocal Microscopy of μ NETs.** A small suspension of μ NETs in 1X PBS was seeded on
9 poly-l-lysine coated slides and imaged using a confocal microscope (Zeiss LSM 510, Carl Zeiss,
10 Inc., USA). Samples were photo-excited at 633 nm, and fluorescence emissions greater than 650
11 nm were collected. We present falsely colored microscopic images of the ICG fluorescence
12 emission (red channel).
13
14
15
16
17
18

19 **Phosphatidylserine characterization by flow cytometry.** RBCs, μ EGs and nEGs were
20 assayed for PS exposure using annexin V labeled with Alexa Fluor488 (AF488) (Invitrogen,
21 Carlsbad, CA). Prior to analysis, each sample was incubated for 30 minutes at room temperature
22 with annexin V conjugate in the presence of a binding buffer, which contained 10 mM HEPES,
23 140 mM NaCl, and 2.5 mM CaCl_2 (pH 7.4). Fluorescence was measured using a BD LSR II flow
24 cytometer (excitation laser: 488 nm, emission filter: 515-545 nm), and the PS-positive populations
25 were quantified using FlowJo V10.
26
27
28
29
30
31
32
33
34

35 **Animal model.** All experiments were conducted under a protocol approved by the Institutional
36 Animal Care and Use Committee, University of California, Irvine (Protocol number AUP-17-074).
37 We implanted a dorsal skinfold window chamber on male mice (25–30 g, C3H strain). Details of
38 the chamber structure and surgical procedure can be found elsewhere.⁷¹ In brief, a mouse was
39 anesthetized with a combination of ketamine and xylazine (2:1 ratio, 0.1/100 g body weight)
40 administered by intraperitoneal injection. A pair of thin titanium window frames (0.4 mm in
41 thickness) was attached to the front and back sides of a dorsal skinfold with 3 screws of 1.5 mm
42 in diameter and 2 sutures. The front layer of the skinfold within the 10 mm circular observation
43 window was removed to expose the subdermal blood vessels in the back layer of the dorsal skinfold,
44
45
46
47
48
49
50
51
52
53
54
55
56
57
58
59
60

1
2
3 which was kept intact to minimize inflammations in the imaging area. Sterile isotonic saline
4 solution was applied onto the exposed skin, followed by placement of a glass cover slip and a
5 retention ring to seal the chamber and protect the subdermis from dehydration and contamination.
6
7

8
9
10 The animal was allowed to recover from anesthesia and surgery on a heating pad. One day after
11 placement of the window chamber, the animal was anesthetized using a mixture of oxygen and 1.5%
12 isoflurane. This method allows a consistent level of anesthesia during the experiment as compared
13 to injection of ketamine and xylazine. The mouse was then placed on the translational stage of an
14 inverted fluorescence microscope (see next subsection for details). Once the animal's body
15 temperature, measured with an NIR thermometer, and respiratory rate were stabilized, a 150 μ L
16 ICG solution or NETs suspension was delivered via retro-orbital injection using a 27.5-gauge
17 insulin syringe. Recording of fluorescence images from the window chamber started immediately
18 before the retro-orbital injection.
19
20
21
22
23
24
25
26
27
28
29

30
31 This model permits *in vivo* longitudinal visualization of blood flow dynamics in sub-dermal
32 blood vessels.⁷²⁻⁷³ It also allows direct determination of the circulation dynamics of a carrier
33 system in blood, such as NETs, in real time without sacrificing the animals at a given time point
34 post-injection. The blood vessels in the window remain visible over an extended time, on the order
35 of two weeks. Therefore, the same animal can be used repeatedly for multiple injections after the
36 injected substance is cleared to minimize data variability when different animals are used.
37
38
39
40
41
42
43

44
45 **In vivo fluorescence imaging.** The experimental setup used to record the fluorescence emission
46 from either free ICG or NETs circulating in the vasculature included a custom-built microscopy
47 system consisting of: (1) an inverted microscope (Diaphot, Nikon Instruments, Melville, NY); (2)
48 an EMCCD camera (QuantEM 512SC, Photometrics, Tucson, AZ); (3) a filter set (49030 ET-
49 INDO GR, Chroma Technology, Bellows Falls, VT); and (4) a 785 nm diode laser (BWF-785-
50
51
52
53
54
55
56
57
58
59
60

1
2
3 450E, B & W Tek, Newark, DE) with a maximum power of 500 mW. The laser beam was
4
5 expanded to a 25 mm diameter spot on the window chamber and the optical intensity was 0.1
6
7 W/cm². The filter set passed emission wavelengths between 815 and 845 nm. The animal was
8
9 placed on a layer of insulation material on the microscope stage, and an air stream incubator (ASI
10
11 400, Nevtek, Williamsville VA) was used to maintain the normal body temperature at 37±1°C. A
12
13 customized fixture with two metal plates was used to hold the window chamber on the translational
14
15 stage. The dermal side of the window faced the objective lens and the epidermal side was
16
17 illuminated with the laser beam.
18
19

20
21 Fluorescence images were acquired over an interval of 60 minutes. During the first 5 minutes,
22
23 images were acquired every second in order to capture the rapid changes in fluorescence intensity.
24
25 During the next 10 minutes, image acquisition interval was every minute. During the final 45
26
27 minutes, images were acquired every five minutes. Spatially-averaged fluorescent intensity in the
28
29 blood vessels (shown as regions of interest (ROI) enclosed by yellow outlines in Figure S2,
30
31 Supporting Information), and the area surrounding the blood vessels within the window chamber
32
33 were quantified using ImageJ. To trace blood vessels, a fluorescence image was first analyzed by
34
35 ImageJ's "Tubeness" plug-in which produces an intermediate image showing how "tube-like" each
36
37 point in the original image is.⁷⁴ Then a threshold was applied to the "Tubeness" image to select
38
39 most of the blood vessels in the image and convert to blood vessel ROI. ROI for the surrounding
40
41 tissue was created by inverting the blood vessel ROI. To evaluate image quality, we quantified the
42
43 signal-to-noise ratio (*SNR*) by the following expression:
44
45
46
47
48

$$49 \quad \text{SNR} = \frac{I_{\text{BV}} - I_{\text{T}}}{\sigma_{\text{T}}} \quad (2)$$

50
51
52
53
54
55
56
57
58
59
60

1
2
3 where I_{BV} is the mean fluorescence intensity in the blood vessels, I_T is the mean fluorescence
4 intensity in tissue surrounding the blood vessels, and σ_T is the standard deviation of fluorescence
5 intensity in the tissue surrounding the blood vessels.
6
7
8
9

10 The diode laser was kept on during the initial 5 minutes of imaging and the window skin
11 temperature was monitored with an infrared camera (A325sc, FLIR, Nashua, NH). The average
12 skin temperature in the window increased slightly from 35.2°C to 35.7°C after 5 minutes of
13 continuous illumination. When the imaging interval was one or five minutes, the diode laser was
14 blocked between each image acquisition to avoid potential skin heating or ICG photobleaching.
15 The total time of laser illumination was approximately 6 minutes. We performed an experiment to
16 confirm that this total time of laser illumination, accumulated intermittently over the course of an
17 experiment, had a negligible effect on the fluorescence intensity (Figure S7, Supporting
18 Information). However, our previous study shows that 3 minutes of cyclic laser irradiation at a
19 much higher intensity (19.7 W/cm²), as compared to the intensity of 0.1 W/cm² used in this study,
20 can result in photo-degradation of NETs.²³
21
22
23
24
25
26
27
28
29
30
31
32
33
34

35 Since the window chamber model allows imaging of the blood vessels over a two weeks period,
36 a single mouse can be used for multiple injections of different or same type of agents. The left or
37 right retro-orbital sinus was used alternatively. Before each injection, a background fluorescence
38 image was recorded to confirm that previously injected fluorophores were eliminated from blood
39 circulation. The injection scheme used in this study is shown in Table S1, Supporting Information.
40 For the images corresponding to dual injection of μ NETs (Figure 5), window chambers were
41 installed on the mouse one day before the second injection. For all other animals receiving two or
42 more injections, window chambers were installed on the mouse one day before the first injection.
43
44
45
46
47
48
49
50
51
52
53
54
55
56
57
58
59
60

1
2
3 **Laser irradiation of the microvasculature.** Laser irradiation was performed on the window
4 (subdermal) side of the preparation. The animal was anesthetized using a mixture of 1.5%
5 isoflurane and oxygen. After anesthesia, blood flow maps were acquired by laser speckle contrast
6 (LSC) imaging, followed by 150 μ L injection of μ NETs into the retro-orbital sinus for the
7 laser+ μ NETs group. At 100 seconds post injection, blood vessels were irradiated with an
8 alexandrite laser (GentleLASE, Candela Corp, Wayland, MA) at a wavelength of 755 nm and
9 pulse duration of 3 ms. The spot size was 10 mm which covered the entire window. Only one laser
10 pulse was delivered to irradiate the blood vessels in the window. For the laser-only group, laser
11 irradiation was performed after blood flow maps were obtained by LSC imaging. Laser pulse
12 energies were measured using an energy meter (FL250A-SH with Nova display, Ophir, Logan,
13 UT).

14
15 LSC imaging was used to determine blood flow dynamics in the window before and ~5 minutes
16 after laser irradiation. During this imaging procedure, the window was trans-illuminated with a
17 continuous wave HeNe laser (632.8 nm, 30 mW), and the resulting speckle pattern produced by
18 the interference of the light waves that scatter from various tissue and blood components in the
19 window was imaged by a CCD camera (10 ms integration time). When blood flow is present,
20 speckle pattern varies with time, resulting in areas of low contrast in the time-integrated images;
21 otherwise, the speckle pattern is static and contrast is high. Ten speckle images were collected,
22 and the contrast was calculated with a sliding-window-based algorithm.⁷⁵ Average contrast was
23 converted to a blood flow index map.⁷⁶

24 ASSOCIATED CONTENT

25 **Supporting Information**

26 Figures S1-S7, Table S1, and Videos S1-S4.

AUTHOR INFORMATION

Corresponding Author

*anvarib@ucr.edu

ABBREVIATIONS

AF488: Alexa Fluor488; CCD: charge-coupled devices; CD47: cluster of differentiation 47; CD55: decay-accelerating factor; CR1: complement receptor type 1; DLS: dynamic light scattering; EGs: erythrocyte ghosts; μ EGs: micro-sized erythrocyte ghosts; nEGs: nano-sized EGs; EMCCD: electron multiplying charge-coupled devices; ICG: indocyanine green; IgE: immunoglobulin E; IL-1: interleukin 1; IL-6: interleukin 6; LSC: laser speckle contrast; NIR: near-infrared; NETs: NIR erythrocyte-derived transducers; μ NETs: micro-sized NETs; nNETs: nano-sized NETs; PBS: phosphate buffered saline; PS: phosphatidylserine; PWSs: port wine stains; RBCs: red blood cells; RhAG: Rh-associated glycoprotein; ROI: regions of interest; SD: standard deviation; SNR: signal-to-noise ratio; TNF: tumor necrosis factor; VEGF: Vascular endothelial growth factor; VEGFR2: VEGF receptor 2;

ACKNOWLEDGEMENTS

This study was supported in part by grants from the National Institute of Arthritis and Musculoskeletal and Skin Diseases (R01-AR068067) and the U. S. National Science Foundation (CBET-1509218). Institutional support from the LAMMP program (NIH: P41EB015890), Beckman Laser Institute Endowment, and the David and Lucile Packard Foundation are also acknowledged.

AUTHOR CONTRIBUTIONS

1
2
3 All authors contributed to various aspects of the experimental design. J.M.B. fabricated and
4 characterized the particles and contributed to the writing of the results section associated with such
5 characterizations. W.J. and B.V. performed the animal experiments. J.C.T. performed the
6 phosphatidylserine characterizations, assisted with particle fabrication and animal experiments.
7
8 R.V. fabricated the particles to assess the effect of laser illumination time on fluorescence emission.
9
10 B.L. and B.C. contributed to the animal model and imaging instruments. J.B. and J.C.T.
11 contributed to the writing of the relevant parts of the methods section. B.A. and W.J. wrote the
12 manuscript.
13
14
15
16
17
18
19
20

21 **COMPETING INTERESTS**

22
23
24 Authors B.A. and R.V. have a financial interest in Radoptics LLC, which is pursuing the
25 commercial development of the particles reported in this manuscript. This interest did not interfere
26 with the scientific work, judgment, and objectivity of the investigators in regards to the
27 experimental procedures, analyses, reporting and interpretation of results, and any other aspect of
28 the study. All the remaining authors declare that they have no conflict of interest.
29
30
31
32
33
34
35

36 **REFERENCES**

- 37
38
39 (1) Peer, D.; Karp, J. M.; Hong, S.; FaroKhazad, O. C.; Margalit, R.; Langer, R. Nanocarriers as an
40 Emerging Platform for Cancer Therapy. *Nat. Nanotechnol.* **2007**, *2* (12), 751-760, DOI:
41 10.1038/nnano.2007.387.
42 (2) Saxena, V.; Sadoqi, M.; Shao, J. Enhanced Photo-Stability, Thermal-Stability and Aqueous-
43 Stability of Indocyanine Green in Polymeric Nanoparticulate Systems. *J. Photochem. Photobiol.*
44 *B, Biol.* **2004**, *74* (1), 29-38, DOI: 10.1016/j.jphotobiol.2004.01.002.
45 (3) Yu, J.; Javier, D.; Yaseen, M. A.; Nitin, N.; Richards-Kortum, R.; Anvari, B.; Wong, M. S.
46 Self-Assembly Synthesis, Tumor Cell Targeting, and Photothermal Capabilities of Antibody-
47 Coated Indocyanine Green Nanocapsules. *JACS* **2010**, *132* (6), 1929-1938, DOI:
48 10.1021/ja908139y.
49 (4) Shemesh, C. S.; Moshkelani, D.; Zhang, H. Thermosensitive Liposome Formulated
50 Indocyanine Green for Near-Infrared Triggered Photodynamic Therapy: In Vivo Evaluation for
51 Triple-Negative Breast Cancer. *Pharm. Res.* **2015**, *32* (5), 1604-1614, DOI: 10.1007/s11095-014-
52 1560-7.
53
54
55
56
57
58
59
60

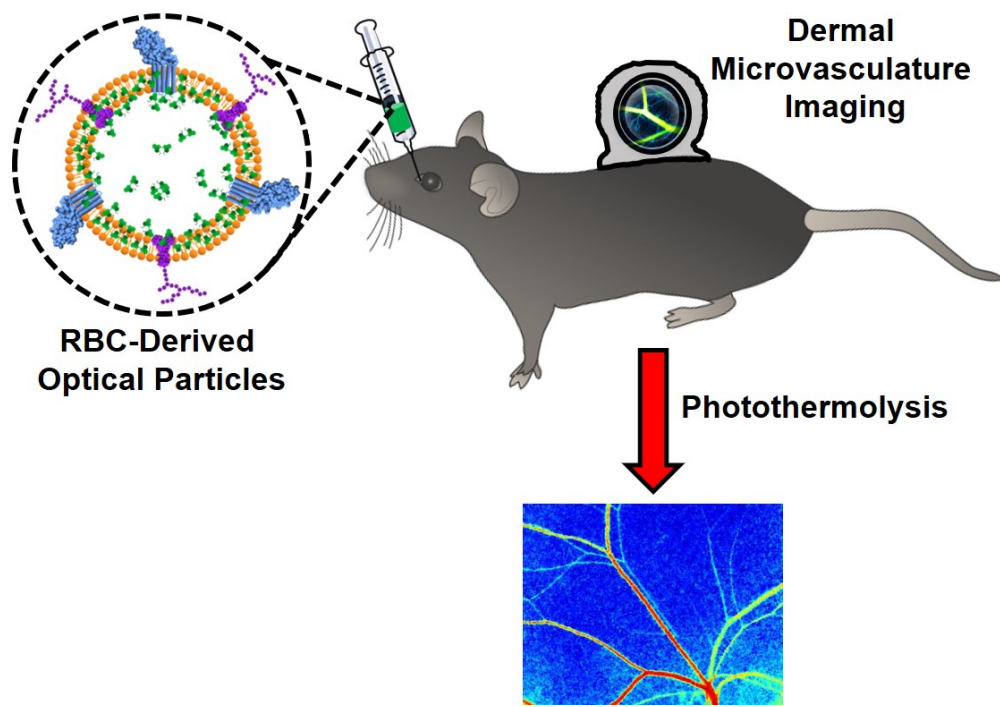
- 1
- 2
- 3
- 4 (5) Guerrero, Y.; Singh, S. P.; Mai, T.; Murali, R. K.; Tanikella, L.; Zahedi, A.; Kundra, V.; Anvari,
5 B. Optical Characteristics and Tumor Imaging Capabilities of Near Infrared Dyes in Free and
6 Nano-Encapsulated Formulations Comprised of Viral Capsids. *ACS Appl. Mater. Interfaces* **2017**,
7 *9* (23), 19601-19611, DOI: 10.1021/acsami.7b03373.
- 8 (6) Jung, B. S.; Rao, A. L. N.; Anvari, B. Optical Nano-Constructs Composed of Genome-Depleted
9 Brome Mosaic Virus Doped with a Near Infrared Chromophore for Potential Biomedical
10 Applications. *ACS Nano* **2011**, *5* (2), 1243-1252, DOI: 10.1021/nn1028696.
- 11 (7) Sheng, Z.; Hu, D.; Xue, M.; He, M.; Gong, P.; Cai, L. Indocyanine Green Nanoparticles for
12 Theranostic Applications. *Nano-Micro Letters* **2013**, *5* (3), 145-150, DOI: 10.5101/nml.v5i3.
- 13 (8) Zhu, H. J.; Cheng, P. H.; Chen, P.; Pu, K. Y. Recent Progress in the Development of Near-
14 Infrared Organic Photothermal and Photodynamic Nanotherapeutics. *Biomater. Sci.* **2018**, *6* (4),
15 746-765, DOI: 10.1039/c7bm01210a.
- 16 (9) Ernsting, M. J.; Murakami, M.; Roy, a.; Li, S.-D. Factors Controlling the Pharmacokinetics,
17 Biodistribution and Intratumoral Penetration of Nanoparticles. *J. Controlled Release* **2013**, *172* (3),
18 782-794, DOI: <https://doi.org/10.1016/j.jconrel.2013.09.013>.
- 19 (10) Jokerst, J. V.; Lobovkina, T.; Zare, R. N.; Gambhir, S. S. Nanoparticle PEGylation for
20 imaging and therapy. *Nanomedicine* **2011**, *6* (4), 715-728, DOI: 10.2217/nmm.11.19.
- 21 (11) ishida, T.; Maeda, R.; Ichihara, M.; Irimura, K.; Kiwada, H. Accelerated Clearance of
22 Pegylated Liposomes in Rats after Repeated Injections. *J. Controlled Release* **2003**, *88* (1), 35-42,
23 DOI: 10.1016/s0168-3659(02)00462-5.
- 24 (12) Armstrong, J. K.; Hempel, G.; Koling, S.; Chan, L. S.; Fisher, T.; Meiselman, H. J.; Garratty,
25 G. Antibody Against Poly(Ethylene Glycol) Adversely Affects Peg-Asparaginase Therapy in
26 Acute Lymphoblastic Leukemia Patients. *Cancer* **2007**, *110* (1), 103-111, DOI:
27 10.1002/cncr.22739.
- 28 (13) Yoo, J.-W.; Chambers, E.; Mitragotri, S. Factors that Control the Circulation Time of
29 Nanoparticles in Blood: Challenges, Solutions and Future Prospects. *Curr. Pharm. Des.* **2010**, *16*
30 (21), 2298-2307.
- 31 (14) Li, J. C.; Zhen, X.; Lyu, Y.; Jiang, Y. Y.; Huang, J. G.; Pu, K. Y. Cell Membrane Coated
32 Semiconducting Polymer Nanoparticles for Enhanced Multimodal Cancer Phototheranostics. *ACS*
33 *Nano* **2018**, *12* (8), 8520-8530, DOI: 10.1021/acsnano.8b04066.
- 34 (15) Zhen, X.; Cheng, P. H.; Pu, K. Y. Recent Advances in Cell Membrane-Camouflaged
35 Nanoparticles for Cancer Phototherapy. *Small* **2019**, *15* (1), DOI: 10.1002/Sml.201804105.
- 36 (16) Muzykantov, V. R. Drug Delivery by Red Blood Cells: Vascular Carriers Designed by Mother
37 Nature. *Expert Opin. Drug Del.* **2010**, *7* (4), 403-427, DOI: 10.1517/17425241003610633.
- 38 (17) Antonelli, A.; Magnani, M. Red Blood Cells as Carriers of Iron Oxide-Based Contrast Agents
39 for Diagnostic Applications. *J. Biomed. Nanotechnol.* **2014**, *10* (9), 1732-1750, DOI:
40 10.1166/jbn.2014.1916.
- 41 (18) Burns, J. M.; Vankayala, R.; Mac, J. T.; Anvari, B. Erythrocyte-Derived Theranostic
42 Nanoplatfoms for Near Infrared Fluorescence Imaging and Photodestruction of Tumors. *ACS*
43 *Appl. Mater. Interfaces* **2018**, *10* (33), 27621-27630, DOI: 10.1021/acsami.8b08005.
- 44 (19) Villa, C. H.; Anselmo, A. C.; Mitragotri, S.; Muzykantov, V. Red Blood Cells: Supercarriers
45 for Drugs, Biologicals, and Nanoparticles and Inspiration for Advanced Delivery Systems. *Adv.*
46 *Drug Delivery Rev.* **2016**, *106*, 88-103, DOI: 10.1016/j.addr.2016.02.007.
- 47 (20) Burns, J. M.; Saager, R.; Majaron, B.; Jia, W.; Anvari, B. Optical Properties of Biomimetic
48 Probes Engineered from Erythrocytes. *Nanotechnology* **2017**, *28* (3), 035101, DOI: 10.1088/1361-
49 6528/28/3/035101.
- 50
- 51
- 52
- 53
- 54
- 55
- 56
- 57
- 58
- 59
- 60

- 1
2
3 (21) Duan, X. P.; Li, Y. P. Physicochemical Characteristics of Nanoparticles Affect Circulation,
4 Biodistribution, Cellular Internalization, and Trafficking. *Small* **2013**, *9* (9-10), 1521-1532, DOI:
5 10.1002/sml.201201390.
- 6 (22) Hong, G.; Antaris, A. L.; Dai, H. Near-Infrared Fluorophores for Biomedical Imaging. *Nat.*
7 *Biomed. Eng.* **2017**, *1*, 0010, DOI: 10.1038/s41551-016-0010.
- 8 (23) Bahmani, B.; Bacon, D.; Anvari, B. Erythrocyte-Derived Photo-Theranostic Agents: Hybrid
9 Nano-Vesicles Containing Indocyanine Green for Near Infrared Imaging and Therapeutic
10 Applications. *Sci. Rep.* **2013**, *3*, 2180, DOI: 10.1038/Srep02180.
- 11 (24) Tang, J. C.; Partono, A.; Anvari, B. Near-Infrared-Fluorescent Erythrocyte-Mimicking
12 Particles: Physical and Optical Characteristics. *IEEE Trans. Biomed. Eng.* **2019**, *66* (4), 1034-1044,
13 DOI: 10.1109/Tbme.2018.2866368.
- 14 (25) Choi, B.; Kang, N. M.; Nelson, J. S. Laser speckle imaging for monitoring blood flow
15 dynamics in the in vivo rodent dorsal skin fold model. *Microvasc. Res.* **2004**, *68* (2), 143-146,
16 DOI: 10.1016/j.mvr.2004.04.003.
- 17 (26) Mohandas, N.; Gallagher, P. G. Red Cell Membrane: Past, Present, and Future. *Blood* **2008**,
18 *112* (10), 3939-3948, DOI: 10.1182/blood-2008-07-161166.
- 19 (27) Daleke, D. L. Regulation of Phospholipid Asymmetry in the Erythrocyte Membrane. *Curr.*
20 *Opin. Hematol.* **2008**, *15* (3), 191-5, DOI: 10.1097/MOH.0b013e3282f97af7.
- 21 (28) Arashiki, N.; Takakuwa, Y.; Mohandas, N.; Hale, J.; Yoshida, K.; Ogura, H.; Utsugisawa, T.;
22 Ohga, S.; Miyano, S.; Ogawa, S.; Kojima, S.; Kanno, H. ATP11C is a Major Flippase in Human
23 Erythrocytes and Its Defect Causes Congenital Hemolytic Anemia. *Haematologica* **2016**, *101* (5),
24 559-565, DOI: 10.3324/haematol.2016.142273.
- 25 (29) Zwaal, R. F.; Comfurius, P.; Bevers, E. M. Surface Exposure of Phosphatidylserine in
26 Pathological Cells. *Cell. Mol. Life Sci.* **2005**, *62* (9), 971-88, DOI: 10.1007/s00018-005-4527-3.
- 27 (30) Fadok, V. A.; Bratton, D. L.; Rose, D. M.; Pearson, A.; Ezekewitz, R. A. B.; Henson, P. M.
28 A Receptor for Phosphatidylserine-Specific Clearance of Apoptotic Cells. *Nature* **2000**, *405*, 85,
29 DOI: 10.1038/35011084.
- 30 (31) Devitt, A.; Moffatt, O. D.; Raykundalia, C.; Capra, J. D.; Simmons, D. L.; Gregory, C. D.
31 Human Cd14 Mediates Recognition and Phagocytosis of Apoptotic Cells. *Nature* **1998**, *392*, 505,
32 DOI: 10.1038/33169.
- 33 (32) Arashiki, N.; Takakuwa, Y. Maintenance and Regulation of Asymmetric Phospholipid
34 Distribution in Human Erythrocyte Membranes: Implications for Erythrocyte Functions. *Curr.*
35 *Opin. Hematol.* **2017**, *24* (3), 167-172, DOI: 10.1097/moh.0000000000000326.
- 36 (33) Boas, F. E.; Forman, L.; Beutler, E. Phosphatidylserine Exposure and Red Cell Viability in
37 Red Cell Aging and in Hemolytic Anemia. *Proc. Natl. Acad. Sci. U.S.A.* **1998**, *95* (6), 3077-3081,
38 DOI: 10.1073/pnas.95.6.3077.
- 39 (34) Schrier, S. L.; Zachowski, A.; Hervé, P.; Kader, J.-C.; Devaux, P. F. Transmembrane
40 Redistribution of Phospholipids of the Human Red Cell Membrane During Hypotonic Hemolysis.
41 *Biochim. Biophys. Acta Biomembr.* **1992**, *1105* (1), 170-176, DOI: 10.1016/0005-2736(92)90176-
42 M.
- 43 (35) Pivkin, I. V.; Peng, Z.; Karniadakis, G. E.; Buffet, P. A.; Dao, M.; Suresh, S. Biomechanics
44 of Red Blood Cells in Human Spleen and Consequences for Physiology and Disease. *Proc. Natl.*
45 *Acad. Sci. U.S.A.* **2016**, *113* (28), 7804-7809, DOI: 10.1073/pnas.1606751113.
- 46 (36) Coker, S. A.; Szczepiorkowski, Z. M.; Siegel, A. H.; Ferrari, A.; Mambrini, G.; Anand, R.;
47 Hartman, R. D.; Benatti, L.; Dumont, L. J. A Study of the Pharmacokinetic Properties and the In
48 Vivo Kinetics of Erythrocytes Loaded With Dexamethasone Sodium Phosphate in Healthy
49
50
51
52
53
54
55
56
57
58
59
60

- 1
2
3 Volunteers. *Transfusion Medicine Reviews* **2018**, *32* (2), 102-110, DOI:
4 10.1016/j.tmry.2017.09.001.
5 (37) Vankayala, R.; Mac, J.; Burns, J. M.; Dunn, E.; Carroll, S.; Bahena, E. M.; Patel, D. K.;
6 Griffey, S.; Anvari, B. Biodistribution and Toxicological Evaluation of Micron- and Nano-Sized
7 Erythrocyte-Derived Optical Particles in Healthy Swiss Webster Mice. *Biomater. Sci.* **2019**, *7*,
8 2123-2133, DOI: 10.1039/C8BM01448E.
9 (38) Wisse, E.; Braet, F.; Luo, D.; De Zanger, R.; Jans, D.; Crabbe, E.; Vermoesen, A. Structure
10 and Function of Sinusoidal Lining Cells in the Liver. *Toxicol. Pathol.* **1996**, *24* (1), 100-111, DOI:
11 10.1177/019262339602400114.
12 (39) Hanayama, R.; Tanaka, M.; Miwa, K.; Nagata, S. Expression of Developmental Endothelial
13 Locus-1 in a Subset of Macrophages for Engulfment of Apoptotic Cells. *J. Immunol.* **2004**, *172*
14 (6), 3876-3882, DOI: DOI 10.4049/jimmunol.172.6.3876.
15 (40) Hanayama, R.; Tanaka, M.; Miwa, K.; Shinohara, A.; Iwamatsu, A.; Nagata, S. Identification
16 of a Factor That Links Apoptotic Cells to Phagocytes. *Nature* **2002**, *417* (6885), 182-187, DOI:
17 Doi 10.1038/417182a.
18 (41) Andersen, M. H.; Berglund, L.; Rasmussen, J. T.; Petersen, T. E. Bovine PAS-6/7 Binds
19 Alpha(V)Beta(5) Integrin and Anionic Phospholipids Through Two Domains. *Biochemistry* **1997**,
20 *36* (18), 5441-5446, DOI: Doi 10.1021/Bi963119m.
21 (42) Otzen, D. E.; Blans, K.; Wang, H. B.; Gilbert, G. E.; Rasmussen, J. T. Lactadherin Binds to
22 Phosphatidylserine-Containing Vesicles in a Two-Step Mechanism Sensitive to Vesicle Size and
23 Composition. *Biochimica Et Biophysica Acta-Biomembranes* **2012**, *1818* (4), 1019-1027, DOI:
24 10.1016/j.bbamem.2011.08.032.
25 (43) Lee, T.-R.; Choi, M.; Kopacz, a. M.; Yun, S.-H.; Liu, W. K.; Decuzzi, P. On the Near-Wall
26 Accumulation of Injectable Particles in the Microcirculation: Smaller is not Better. *Sci. Rep.* **2013**,
27 *3*, 2079, DOI: 10.1038/srep02079.
28 (44) Fish, M. B.; Fromen, C. A.; Lopez-Cazares, G.; Golinski, A. W.; Scott, T. F.; Adili, R.;
29 Holinstat, M.; Eniola-Adefeso, O. Exploring Deformable Particles in Vascular-Targeted Drug
30 Delivery: Softer is Only Sometimes Better. *Biomaterials* **2017**, *124*, 169-179, DOI:
31 <https://doi.org/10.1016/j.biomaterials.2017.02.002>.
32 (45) Fadok, V. A.; Bratton, D. L.; Rose, D. M.; Pearson, A.; Ezekewitz, R. A.; Henson, P. M. A
33 receptor for Phosphatidylserine-Specific Clearance of Apoptotic Cells. *Nature* **2000**, *405* (6782),
34 85-90, DOI: 10.1038/35011084.
35 (46) Setty, B. N. Y.; Betal, S. G. Microvascular Endothelial Cells Express a Phosphatidylserine
36 Receptor: a Functionally Active Receptor for Phosphatidylserine-Positive Erythrocytes. *Blood*
37 **2008**, *111* (2), 905-914, DOI: 10.1182/blood-2007-07-099465.
38 (47) Manodori, A. B.; Barabino, G. A.; Lubin, B. H.; Kuypers, F. A. Adherence of
39 Phosphatidylserine-Exposing Erythrocytes to Endothelial Matrix Thrombospondin. *Blood* **2000**,
40 *95* (4), 1293-1300.
41 (48) Borst, O.; Abed, M.; Alesutan, I.; Towhid, S. T.; Qadri, S. M.; Foller, M.; Gawaz, M.; Lang,
42 F. Dynamic Adhesion of Eryptotic Erythrocytes to Endothelial Cells via CXCL16/SR-PSOX. *Am.*
43 *J. Physiol., Cell Physiol.* **2012**, *302* (4), C644-51, DOI: 10.1152/ajpcell.00340.2011.
44 (49) Wautier, M. P.; Heron, E.; Picot, J.; Colin, Y.; Hermine, O.; Wautier, J. L. Red Blood Cell
45 Phosphatidylserine Exposure is Responsible for Increased Erythrocyte Adhesion to Endothelium
46 in Central Retinal Vein Occlusion. *J. Thromb. Haemost.* **2011**, *9* (5), 1049-1055, DOI:
47 10.1111/j.1538-7836.2011.04251.x.
48
49
50
51
52
53
54
55
56
57
58
59
60

- 1
2
3 (50) Fens, M. H. A. M.; van Wijk, R.; Andringa, G.; van Rooijen, K. L.; Dijkstra, H. M.;
4 Rasmussen, J. T.; de Vooght, K. M. K.; Schifflers, R. M.; Gaillard, C. A. J. M.; van Solinge, W.
5 W. A role for Activated Endothelial Cells in Red Blood Cell Clearance: Implications for
6 Vasopathology. *Haematol. Hematol. J.* **2012**, *97* (4), 500-508, DOI:
7 10.3324/haematol.2011.048694.
8
9 (51) Sumpio, B. E.; Riley, J. T.; Dardik, A. Cells in Focus: Endothelial Cell. *Int. J. Biochem. Cell*
10 *Biol.* **2002**, *34* (12), 1508-1512, DOI: 10.1016/S1357-2725(02)00075-4.
11 (52) Weis, S. M.; Cheresch, D. A. Pathophysiological Consequences of Vegf-Induced Vascular
12 Permeability. *Nature* **2005**, *437* (7058), 497-504, DOI: 10.1038/nature03987.
13 (53) Roberts, W. G.; Palade, G. E. Increased Microvascular Permeability and Endothelial
14 Fenestration Induced by Vascular Endothelial Growth-Factor. *J. Cell Sci.* **1995**, *108*, 2369-2379.
15 (54) Ferrara, N.; Gerber, H. P.; LeCouter, J. The Biology of VEGF and its Receptors. *Nat. Med.*
16 **2003**, *9* (6), 669-676, DOI: Doi 10.1038/Nm0603-669.
17 (55) Dejana, E. Endothelial Cell-Cell Junctions: Happy Together. *Nat. Rev. Mol. Cell Biol.* **2004**,
18 *5* (4), 261-270, DOI: 10.1038/nrm1357.
19 (56) Long, Y. M.; Zhao, X. C.; Clermont, A. C.; Zhou, Q. F.; Liu, Q.; Feener, E. P.; Yan, B.; Jiang,
20 G. B. Negatively Charged Silver Nanoparticles Cause Retinal Vascular Permeability by Activating
21 Plasma Contact System and Disrupting Adherens Junction. *Nanotoxicology* **2016**, *10* (4), 501-511,
22 DOI: 10.3109/17435390.2015.1088589.
23 (57) Setyawati, M. I.; Tay, C. Y.; Chia, S. L.; Goh, S. L.; Fang, W.; Neo, M. J.; Chong, H. C.; Tan,
24 S. M.; Loo, S. C. J.; Ng, K. W.; Xie, J. P.; Ong, C. N.; Tan, N. S.; Leong, D. T. Titanium Dioxide
25 Nanomaterials Cause Endothelial Cell Leakiness by Disrupting the Homophilic Interaction of Ve-
26 Cadherin. *Nat. Commun.* **2013**, *4*, 1673, DOI: 10.1038/Ncomms2655.
27 (58) Reid, M.; Takakuwa, Y.; Conboy, J.; Tchernia, G.; Mohandas, N. Glycophorin C Content of
28 Human Erythrocyte Membrane is Regulated by Protein 4.1. *Blood* **1990**, *75* (11), 2229-2234.
29 (59) Nicolas, V.; Le Van Kim, C.; Gane, P.; Birkenmeier, C.; Cartron, J.-P.; Colin, Y.; Mouro-
30 Chanteloup, I. Rh-RhAG/Ankyrin-R, a New Interaction Site between the Membrane Bilayer and
31 the Red Cell Skeleton, is Impaired by Rnull-associated Mutation. *J. Biol. Chem.* **2003**, *278* (28),
32 25526-25533, DOI: 10.1074/jbc.M302816200.
33 (60) Manno, S.; Takakuwa, Y.; Mohandas, N. Identification of a Functional Role for Lipid
34 Asymmetry in Biological Membranes: Phosphatidylserine-Skeletal Protein Interactions Modulate
35 Membrane Stability. *Proc. Natl. Acad. Sci. U.S.A.* **2002**, *99* (4), 1943-1948, DOI:
36 10.1073/pnas.042688399.
37 (61) Johnson, C. P.; Tang, H.-Y.; Carag, C.; Speicher, D. W.; Discher, D. E. Forced Unfolding of
38 Proteins Within Cells. *Science* **2007**, *317* (5838), 663-666, DOI: 10.1126/science.1139857.
39 (62) Safeukui, I.; Buffet, P. A.; Perrot, S.; Sauvanet, A.; Aussilhou, B.; Dokmak, S.; Couvelard,
40 A.; Hatem, D. C.; Mohandas, N.; David, P. H.; Mercereau-Puijalon, O.; Milon, G. Surface Area
41 Loss and Increased Sphericity Account for the Splenic Entrapment of Subpopulations of
42 Plasmodium falciparum Ring-Infected Erythrocytes. *PLoS One* **2013**, *8* (3), e60150, DOI:
43 10.1371/journal.pone.0060150.
44 (63) Lu, T.; Mac, J. T.; Tweini, R.; Tran, K.; Vankayala, R.; Anvari, B. Mechanical
45 Characterization of Erythrocyte-Derived Optical Microparticles by Quantitative Phase Imaging
46 and Optical Tweezers, SPIE: 2019; Vol. 10887, Quantitative Phase Imaging V, Proc. SPIE.,
47 (64) Cokelet, G. R.; Meiselman, H. J. Rheological Comparison of Hemoglobin Solutions and
48 Erythrocyte Suspensions. *Science* **1968**, *162* (3850), 275-277, DOI: 10.1126/science.162.3850.275.
49
50
51
52
53
54
55
56
57
58
59
60

- 1
2
3 (65) Mohandas, N.; Chasis, J. A. Red Blood Cell Deformability, Membrane Material Properties
4 and Shape: Regulation by Transmembrane, Skeletal and Cytosolic Proteins and Lipids. *Semin.*
5 *Hematol.* **1993**, *30* (3), 171-192.
- 6 (66) Baumler, H.; Neu, B.; Donath, E.; Kiesewetter, H. Basic Phenomena of Red Blood Cell
7 Rouleaux Formation. *Biorheology* **1999**, *36* (5-6), 439-42.
- 8 (67) Weisel, J. W.; Litvinov, R. I. Red Blood Cells: the Forgotten Player in Hemostasis and
9 Thrombosis. *J. Thromb. Haemost.* **2019**, *17* (2), 271-282, DOI: doi:10.1111/jth.14360.
- 10 (68) Baumler, H.; Neu, B.; Mitlohner, R.; Georgieva, R.; Meiselman, H. J.; Kiesewetter, H.
11 Electrophoretic and Aggregation Behavior of Bovine, Horse and Human Red Blood Cells in
12 Plasma and in Polymer Solutions. *Biorheology* **2001**, *38* (1), 39-51.
- 13 (69) Jacques, S. L. Optical Properties of Biological Tissues: a Review. *Phys. Med. Biol.* **2013**, *58*
14 (11), R37-R61, DOI: 10.1088/0031-9155/58/11/r37.
- 15 (70) Burns, J. M.; Jia, W.; Nelson, J. S.; Majaron, B.; Anvari, B. Photothermal Treatment of Port-
16 Wine Stains Using Erythrocyte-Derived Particles Doped with Indocyanine Green: a Theoretical
17 Study. *J. Biomed. Opt.* **2018**, *23* (12), 121616, DOI: 10.1117/1.Jbo.23.12.121616.
- 18 (71) Moy, A. J.; White, S. M.; Indrawan, E. S.; Lotfi, J.; Nudelman, M. J.; Costantini, S. J.;
19 Agarwal, N.; Jia, W.; Kelly, K. M.; Sorg, B. S.; Choi, B. Wide-Field Functional Imaging of Blood
20 Flow and Hemoglobin Oxygen Saturation in the Rodent Dorsal Window Chamber. *Microvasc.*
21 *Res.* **2011**, *82* (3), 199-209.
- 22 (72) Menger, M. D.; Laschke, M. W.; Vollmar, B. Viewing the Microcirculation Through the
23 Window: Some Twenty Years Experience with the Hamster Dorsal Skinfold Chamber. *Eur. Surg.*
24 *Res.* **2002**, *34* (1-2), 83-91.
- 25 (73) Choi, B.; Jia, W.; Channual, J.; Kelly, K. M.; Lotfi, J. The Importance of Long-Term
26 Monitoring to Evaluate the Microvascular Response to Light-Based Therapies. *J. Invest. Dermatol.*
27 **2008**, *128* (2), 485-488.
- 28 (74) Sato, Y.; Nakajima, S.; Shiraga, N.; Atsumi, H.; Yoshida, S.; Koller, T.; Gerig, G.; Kikinis,
29 R. Three-Dimensional Multi-Scale Line Filter for Segmentation and Visualization of Curvilinear
30 Structures in Medical Images. *Med Image Anal* **1998**, *2* (2), 143-68.
- 31 (75) Dunn, A. K.; Bolay, T.; Moskowitz, M. A.; Boas, D. A. Dynamic Imaging of Cerebral Blood
32 Flow Using Laser Speckle. *J. Cereb. Blood Flow Metab.* **2001**, *21* (3), 195-201, DOI: Doi
33 10.1097/00004647-200103000-00002.
- 34 (76) Ramirez-San-Juan, J. C.; Ramos-Garcia, R.; Guizar-Iturbide, I.; Martinez-Niconoff, G.; Choi,
35 B. Impact of Velocity Distribution Assumption on Simplified Laser Speckle Imaging Equation.
36 *Opt. Express* **2008**, *16* (5), 3197-3203, DOI: Doi 10.1364/Oe.16.003197.
- 37
38
39
40
41
42
43
44
45
46
47
48
49
50
51
52
53
54
55
56
57
58
59
60



31 Optical particles derived from red blood cells for phototheranostics of cutaneous vasculature in mice

32
33 94x71mm (300 x 300 DPI)